Investigation of Anisotropy-Resolving Turbulence Models by Reference to Highly-Resolved LES Data for Separated Flow

Y.J. JANG[1], M.A. LESCHZINER[1], K. ABE[2] and L. TEMMERMAN[1]
[1]*Department of Aeronautics, Imperial College, London SW7 2BY, U.K.*
[2]*Department of Aeronautics and Astronautics, Kyushu University, Fukuoka, Japan*

Abstract. The predictive properties of several non-linear eddy-viscosity models are investigated by reference to highly-resolved LES data obtained by the authors for an internal flow featuring massive separation from a curved surface. The test geometry is a periodic segment of a channel constricted by two-dimensional (2D) 'hills' on the lower wall. The mean-flow Reynolds number is 21560. Periodic boundary conditions are applied in the streamwise and spanwise directions. This makes the statistical properties of the simulated flow genuinely 2D and independent from boundary conditions, except at the walls. The simulation was performed on a high-quality, 5M-node grid. The focus of the study is on the exploitation of the LES data for the mean-flow, Reynolds stresses and macro-length-scale. Model solutions are first compared with the LES data, and selected models are then subjected to *a-priori* studies designed to elucidate the role of specific model fragments in the non-linear stress-strain/vorticity relation and their contribution to observed defects in the mean-flow and turbulence fields. The role of the equation governing the length-scale, via different surrogate variables, is also investigated. It is shown that, while most non-linear models overestimate the separation region, due mainly to model defects that result in insufficient shear stress in the separated shear layer, model forms can be derived which provide a satisfactory representation of the flow. One such model is identified. This combines a particular quadratic constitutive relation with a wall-anisotropy term, a high-normal-strain correction and a new form of the equation for the specific dissipation $\omega = \varepsilon/k$.

Key words: large eddy simulation, non-linear eddy-viscosity models, separation, turbulence modelling.

1. Introduction

Predictive inadequacies of linear eddy-viscosity models, observed over many years in computations for complex flows, have motivated the development and application of second-moment closure and non-linear eddy-viscosity models. Both model types are able, in principle, to resolve Reynolds-stress anisotropy, the effects of flow curvature on turbulence and the correct sensitivity of turbulence to irrotational straining. While second-moment closure offers a fundamentally strong modelling foundation, the quest for model simplicity, computational economy and numerical robustness has led to recent research being focused, principally, on the formula-

tion of improved non-linear eddy-viscosity and explicit algebraic Reynolds-stress models (NLEVM, EARSM). Several new model forms or variants of older models have been proposed in recent years, among them those of Gatski and Speziale [1], Craft et al. [2], Apsley and Leschziner [3], Rung et al. [4], Wallin and Johansson [5] and Abe et al. [6].

Despite substantial efforts being expended on model validation, there continues to be much uncertainty on the predictive qualities of NLEVMs in complex flows. In part, this is because a reliable assessment of models by reference to experimental data poses a number of problems unrelated to the models themselves and their numerical implementation. Issues of principal concern are (i) the compatibility of the computational implementation with the experimental conditions, (ii) the completeness and accuracy of the boundary conditions and (iii) the accuracy of the data used to assess the predictions obtained with the model. The first item is concerned with flow dimensionality, directional homogeneity and symmetry. For example, there are often inescapable differences between statistically 2D computations, usually undertaken in efforts to elucidate fundamental characteristics of turbulence models, and data for nominally 2D experimental configurations used to validate the computations. Unless the spanwise extent of the flow in question approaches infinity or the flow is perfectly axisymmetric (in a statistical sense), there will always be some contamination by 3D straining, which may have disproportionately large effects on the nominally 2D flow quantities. Incompleteness and errors in respect of boundary conditions, especially in relation to turbulence quantities (e.g. Reynolds stresses and dissipation rate) is another important source of uncertainty and may be sufficiently serious to invalidate conclusions derived from a validation study.

The above issues are especially pertinent to studies of flows that involve separation from curved surfaces, a process that is extremely sensitive to spanwise distortions, geometric imperfections and inaccuracies in the prescription of boundary conditions. Examples are collaborative validation studies for separated flow around high-lift and transonic aerofoils [7, 8], over hill-shaped bumps on a wavy wall [9], around highly-loaded blades [10] and in diffusers [11]. In some of these studies, uncertainties were severe enough to prevent any sensible conclusion being reached on the inherent predictive characteristics of the models tested. In other cases, it was only due to a closely interactive and iterative sequence of computational campaigns and the use of more than one set of data that a reasonable level of confidence on model performance could be attained.

A potentially far more reliable route for investigating turbulence models, especially as a pre-cursor to their improvement, is to use highly resolved LES (or DNS) data in circumstances that hardly pose any uncertainties in respect of 3D features and boundary conditions. Appropriate simulations, if carefully undertaken and verifiably accurate, can yield data that are superior and far more detailed than those derived from experiments. In particular, such simulations yield data on budgets of turbulent stresses, which differentiate the various transportive and generative
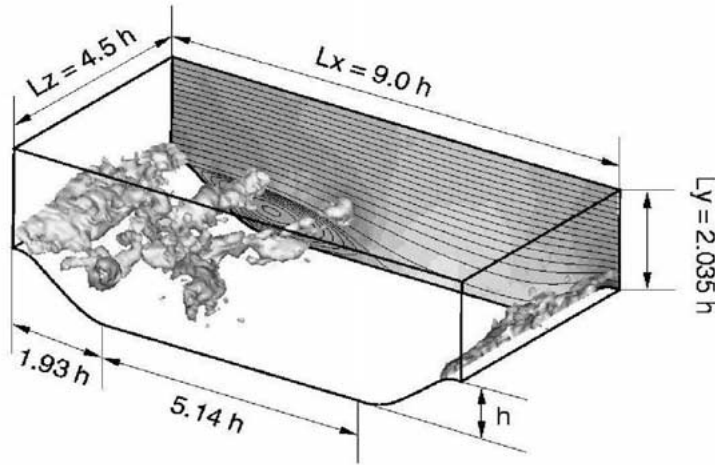
Figure 1. Periodic hill geometry under consideration, including LES realizations of pressure contours and time-mean stream-function contours.

mechanisms. Thus, *a-priori* studies can be undertaken on the validity of model fragments for particular physical processes for which there are exact equivalents that can be extracted from the data. While DNS data have been used extensively, for over a decade, as an aid to turbulence closure, the scope and usefulness of this input has been constrained by the low Reynolds number of the simulated flows, dictated by resource limitations, and the simplicity of the flows (mainly homogenous strain, channel flow, boundary layers and free shear layers). Increasingly, however, Large Eddy Simulation, undertaken for complex geometries over sufficiently fine, high-quality grids at moderately high Reynolds numbers, are able to provide sufficiently accurate data for reliable model assessment in challenging flow conditions. While subgrid-scale modelling and near-wall resolution are, generally, issues that affect accuracy, the use of sufficiently fine grids can be made to render both practically insignificant, at least in terms of the present exploitation of the data for model validation.

The present paper is concerned with investigating NLEVMs by reference to highly resolved LES data, obtained for the geometry shown in Figure 1. This is a streamwise-periodic segment of a channel constrained by 2D 'hills' which provoke massive separation on their leeward sides. The flow, at Reynolds number 21560, based on the channel flow rate (or 10595, based on hill height and mean velocity above the hill crest), is free from transitional features and is, effectively, fully turbulent over approximately 90% of its transverse (wall-to-wall) extent. At the same time, the Reynolds number is sufficiently low to have allowed the semi-viscous *lower* near-wall layer to be resolved with a high-quality mesh down to $y^+ = O(1)$. While the grid was coarser at the upper wall, with $y^+ = O(15)$ along the near-wall grid plane, the flow along that wall is close to equilibrium and its near-wall resolution (effected with appropriate wall laws) had a very minor effect on the

separation process. Apart from offering a comprehensive database, this test case has a number of important advantages for the present purpose of model investigation. First, separation takes place from a curved surface – an especially challenging feature for turbulence models, and one that has a strong effect on the reattachment position. Second, because of streamwise periodicity, the solution is not 'anchored' to inlet conditions, a situation that increases the sensitivity of the predictions to the quality of the turbulence model. Third, the flow is truly statistically 2D, without any contamination associated with secondary motion arising from spanwise confinement. Finally, the geometry allows for a significant post-reattachment recovery region on the flat plate separating successive hill. The importance of this last feature lies in the fact that most turbulence models that return the correct recirculation-zone dimensions in separated flow also give rise to an insufficient recovery in the post-reattachment wake.

The LES data used herein arise from simulations undertaken by Temmerman and Leschziner [12]. Their reliability has been confirmed by parallel simulations by Mellen et al. [13] with an entirely different LES code. The results of the two simulation are very close, as is shown by Temmerman et al. [14]. LES computations in the last-named study also illustrate the strong dependence of the whole flow on the separation behaviour. For example, a change in the separation location of Δ is shown to result in a change of order 7Δ in the reattachment point. This is indicative of the high sensitivity of gross features of the flow to minor perturbations.

In the present paper, the performance of various models is not merely assessed by reference to the LES solution, but *a-priori* studies are reported that investigate the contribution of various elements of the models, in particular that of additive fragments in the non-linear stress-strain relationship. Such studies allow more insight to be gained into the question of which fragments are more likely than others to be the cause of errors and what steps need to be taken to rectify the errors.

2. The Simulation

The simulation of the flow shown in Figure 1 is not the central aspect of this paper. Hence, only some key facts are conveyed here. Details may be found in [12].

The simulation was performed over a grid of approximately 5M nodes, covering a spanwise slab of 4.5 hill heights. The mesh was close to orthogonal, of low aspect ratio and with mesh-expansion ratio below 1.05. The y^+-value at the nodes closest to the lower wall was around 0.5, allowing the no-slip condition to be used directly. For reasons of economy, the y^+-values at the nodes closest to the upper wall were arranged to be of order 15, necessitating the use of a wall function that was based on a 1/7th-power-law assumption for the (time-varying) near-wall velocity. Temmerman et al. [14] show that the choice of an appropiate wall function is far superior to the prescription of a no-slip condition when the wall-nearest nodes are in the buffer region and/or outside the semi-viscous sublayer. While the treatment at the upper wall has no appreciable effect on the quality of the simulation in the lower flow re-

gion, it clearly precludes a correct representation of the wall-asymptotic behaviour of the Reynolds stresses in the viscous sublayer. Subgrid-scale (SGS) effects were approximated with the WALE model Ducros [15], giving SGS viscosity values below the fluid viscosity over most of the flow domain. The ratio of Kolmogorov scale to cell-size was below 10 over most of the simulation domain. Statistical data were assembled over a period of 55 flow-through times, at a cost of approximately 50,000 processor hours on a Cray T3E computer. A similar simulation, for the same geometry and precisely the same grid, but with a different subgrid-scale model, was performed by Mellen et al. [13], and this gave results very close to those obtained by Temmerman and Leschziner. Separation is predicted at $x/h = 0.22$ and reattachment at 4.72, and both are in close agreement with the data by Mellen et al. Adherence to realizability constraints has been verified, specifically in terms of the relationship between the second and third invariants of the stress-anisotropy tensor

$$A_2 \equiv a_{ij}a_{ij}; \quad A_3 \equiv a_{ik}a_{kl}a_{li}, \tag{1}$$

where

$$a_{ij} \equiv \frac{\overline{u_i u_j}}{k} - \frac{2}{3}\delta_{ij}.$$

The model-predicted behaviour of these invariants, especially in the near-wall region, plays a significant role in judging the properties of alternative model forms. Stress-transport budgets have been extracted from the simulation, and these are being used elsewhere for *a-priori* studies of second-moment-closure models.

3. Turbulence Modelling

In the description to follow, Cartesian tensors of rank 2 are identified by bold symbols (e.g. $\mathbf{a}$), and their components are italicized (e.g. a_{ij}). Contracted products are written as for matrix multiplication:

$$\mathbf{ab} = a_{ik}b_{kj}, \quad \mathbf{abc} = a_{ik}b_{kl}c_{li}, \quad \text{etc.} \tag{2}$$

The trace, a_{kk} of a tensor is denoted by $\{\mathbf{a}\}$. Components of mean velocity are denoted by U_i and turbulent fluctuation by u_i. The turbulent kinetic energy is $k = (1/2)\overline{u_i u_i}$, the unit tensor is $\mathbf{I} = \delta_{ij}$ and the dimensionless mean strain $\mathbf{s}$ and vorticity $\mathbf{w}$ tensors are, respectively,

$$s_{ij} = \frac{\tau}{2}\left(\frac{\partial U_i}{\partial x_j} + \frac{\partial U_j}{\partial x_i} - \frac{2}{3}\frac{\partial U_k}{\partial x_k}\delta_{ij}\right), \quad w_{ij} = \frac{\tau}{2}\left(\frac{\partial U_i}{\partial x_j} - \frac{\partial U_j}{\partial x_i}\right). \tag{3}$$

For the present incompressible flow, $\partial U_k/\partial x_k = 0$. The turbulent time-scale τ is

$$\tau = \begin{cases} \dfrac{k}{\varepsilon} & (k\text{–}\varepsilon \text{ models}), \\[2ex] \dfrac{1}{\beta^*\omega} & (k\text{–}\omega \text{ models}), \end{cases} \tag{4}$$

where β^* is either a constant or a function of the turbulent Reynolds number $R_w = k/\nu\omega$ (see [16]).

The general constitutive relationship between the Reynolds stresses and the mean strain for incompressible flow was proposed by Pope [17]. Considering at most a cubic constitutive relationship, the Reynolds stresses can be written in the following canonical form:

$$
\begin{aligned}
\mathbf{a} \;=\; & -2C_\mu\mathbf{s} + q_1\left(\mathbf{s}^2 - \frac{1}{3}\{\mathbf{s}^2\}\mathbf{I}\right) + q_2(\mathbf{ws} - \mathbf{sw}) + q_3\left(\mathbf{w}^2 - \frac{1}{3}\{\mathbf{w}^2\}\mathbf{I}\right) \\
& - \gamma_1\{\mathbf{s}^2\}\mathbf{s} - \gamma_2\{\mathbf{w}^2\}\mathbf{s} - \gamma_3\left(\mathbf{w}^2\mathbf{s} + \mathbf{sw}^2 - \{\mathbf{w}^2\}\mathbf{s} - \frac{2}{3}\{\mathbf{wsw}\}\mathbf{I}\right) \\
& - \gamma_4(\mathbf{ws}^2 - \mathbf{s}^2\mathbf{w}),
\end{aligned}
\tag{5}
$$

where $\{\mathbf{s}^2\} = s_{ij}s_{ij}$ and $\{\mathbf{w}^2\} = -w_{ij}w_{ij}$ are the dimensionless strain and vorticity invariants, respectively. For 2D flow, relation (5) reduces to a (tensorially) quadratic form, as $\gamma_3 = \gamma_4 = 0$. While the terms associated with γ_1 and γ_2 arise from cubic bases (and will be referred to as 'quasi-cubic' in discussions to follow), they are, in fact, tensorially linear, because $\{\mathbf{s}^2\}$ and $\{\mathbf{w}^2\}$ are scalars. Hence, these terms, which can be shown to represent the effects of curvature-related strain on the stresses, may be viewed as additive corrections to C_μ. All non-linear eddy-viscosity models are tensorially quadratic in 2D flow. Differences in order (third or fourth) only arise in 3D conditions, and these originate from differences in the derivation of relations of the form (5) and particular truncation choices.

Models that relate τ to k and ε, make use of the related turbulence-transport equations:

$$
\frac{Dk}{Dt} = \nabla \cdot \left[\left(\nu + \frac{\nu_t}{\sigma_k}\right)\nabla k\right] + (P - \tilde\varepsilon - D),
\tag{6}
$$

$$
\frac{D\tilde\varepsilon}{Dt} = \nabla \cdot \left[\left(\nu + \frac{\nu_t}{\sigma_\varepsilon}\right)\nabla\tilde\varepsilon\right] + (C_{\varepsilon 1}f_1 P - C_{\varepsilon 2}f_2\tilde\varepsilon)\frac{\tilde\varepsilon}{k} + S_\varepsilon,
\tag{7}
$$

where $\nu_t = C_\mu(k^2/\tilde\varepsilon)$. In the above, $\tilde\varepsilon$ is the homogeneous dissipation rate which is related to the actual dissipation ε through $\tilde\varepsilon = \varepsilon - D$, where

$$
D = 2\nu\left(\frac{\partial k^{1/2}}{\partial x_i}\right)^2.
$$

Additional source terms, deemed collected in S_ε, may be included to control the growth of the turbulent length-scale and to procure the correct behaviour of the near-wall viscous sublayer.

Models that use the specific dissipation ω make use of the following transport equations [16]:

$$
\frac{Dk}{Dt} = \nabla \cdot \left[\left(\nu + \frac{\nu_t}{\sigma_k}\right)\nabla k\right] + (P - \beta^*\omega k),
\tag{8}
$$

$$\frac{D\omega}{Dt} = \nabla \cdot \left[\left(\nu + \frac{\nu_t}{\sigma_\omega} \right) \nabla \omega \right] + \frac{\alpha}{\nu_t} P - \beta \omega^2 + S_\omega, \qquad (9)$$

where $\nu_t = \alpha^*(k/\omega)$ and α^* is a constant or a function of the turbulent Reynolds number R_w or an equivalent universal wall distance. As will be explained below, there are considerable (and influential) differences between variants of Equation (9) used in different ω-based models. These include the use of different constants, damping functions and fragments in S_ω, the last rooted in the transformation of the ω-equation from that governing ε.

Five NLEVMs are investigated herein, namely:

- the Gatski and Speziale [1] model (GS-ε),
- the Craft et al [2] model (CLS-ε),
- the Apsley and Leschziner [3] model (AL-ε),
- the Wallin and Johansson [5] model – two variants (WJ-ε, WJ-ω),
- the Abe et al. model [6] (AJL-ω).

In the above model abbreviations, the extensions ε and ω indicate the nature of the length-scale equation used in the models. The NLEVMs are compared to two linear baseline models: the k–ε model of Launder and Sharma [18] (LS-ε) and the k–ω model of Wilcox [16] (WX-ω). Other NLEVM variations have been examined – for example, such involving the use of different length-scale equations or additional realizability constraints – and related comments on the observed predictive behaviour will be made, as appropriate, without the background of reported results. The first three models and one variant of the WJ model use the ε-equation, while the second variant of the WJ model and the last model include different forms of the ω-equation. The following brief subsections summarize the key features of the models, while Appendix A provides a tabular statement of model-specific coefficients, damping functions and additive terms.

3.1. THE GATSKI AND SPEZIALE MODEL (GS) [1]

This is a high-Re k–ε model, originally proposed by Gatski and Speziale [1] and later 'regularized' by Speziale and Xu [19] to circumvent the singular behaviour observed in certain complex-strain conditions. The model was derived from the weak-equilibrium (zero-anisotropy transport) form of the Reynolds-stress equations and then transformed into an explicit set of relations for the Reynolds stresses, on the assumption that the ratio P_k/ε is given or otherwise determinable. In this model, $\gamma_1 - \gamma_4 = 0$, the remaining coefficients being functions of various powers (up to 6) of the strain and vorticity invariants. A seemingly minor but influential feature of the model, rooted in observations of the performance Wilcox's ω-equation, is that the separation between the ε-equation constants, $C_{\varepsilon 1} = 1.44$, $C_{\varepsilon 2} = 1.83$, is smaller than the standard, which favours separation in boundary layers subjected to an adverse pressure gradient. These coefficients have subsequently

been adopted in other models – for example, those of Apsley and Leschziner [3] and Abe et al. [6]. The model has been used here in conjunction with conventional log-law-based wall laws, which divide the near-wall region into a fully viscous sublayer and a fully turbulent layer above it and which involve the use of cell-integrated turbulence production and dissipation for the k- and ε-equations solved over the near-wall cell.

3.2. THE CRAFT, LAUNDER AND SUGA MODEL (CLS) [2]

This is the first low-Re 'cubic' k–ε model proposed, and it was designed with particular attention paid to the representation of viscous near-wall processes, although it will be shown later that the model misrepresents the near-wall anisotropy. Hence, its constants are functions of the turbulent Reynolds number, in addition to strain and vorticity invariants. The functional dependence $C_\mu(\{\mathbf{s}^2\}, \{\mathbf{w}^2\})$ was calibrated by reference to DNS data for homogeneously strained flow. There are two versions of this model, one using the k- and ε-equations and the other a third transport equation for the second invariant of the Reynolds-stress tensor $a_{ij}a_{ij}$. Here, the former variant has been used, but this is known (e.g. [20]) not to give the correct separation between the normal stresses at the wall. It is significantly simpler, however, and widely used as a representative variant of the category of cubic models. An influential feature of the model is its use of the length-scale correction,

$$S_l = \max\left[0.83(\gamma - 1)\gamma^2\frac{\tilde{\varepsilon}}{k}, 0\right], \quad \gamma = \frac{k^{3/2}}{c_l\tilde{\varepsilon}y_n}, \quad c_l = 2.5 \tag{10}$$

in the ε-equation. This term, relating to an earlier proposal by Yap [21], is designed to depress the length-scale returned by the ε-equation towards its equilibrium variation $c_l y_n$. By doing so, it reduces the eddy viscosity near the wall and favours separation when the boundary layer is subjected to an adverse pressure gradient.

3.3. THE APSLEY AND LESCHZINER MODEL (AL) [3]

This 'cubic' low-Re model, originally used in conjunction with the ε-equation, was derived from the zero-transport form of Reynolds-stress equations, with the addition of a number of further simplifications. Thus, the explicit cubic stress-strain/vorticity relationship was obtained through a two-step iterative substitution of the implicit algebraic relationships implied by the parent Reynolds-stress model. The model coefficients were then determined as function of y_n^* $(= y_n\sqrt{k}/\nu)$ by reference to DNS data for a number of near-wall flows, so as to ensure that a broadly correct normal-stress separation is returned in the near-wall layer. Finally, functional corrections were introduced to account for non-equilibrium conditions $P_k/\varepsilon \neq 1$. In common with the model of Gatski and Speziale [1], the present model also uses $C_{\varepsilon 1} = 1.44$ and $C_{\varepsilon 2} = 1.83$ in the ε-equation. As noted earlier, this

enhances the tendency towards separation in the presence of an adverse pressure gradient.

3.4. THE WALLIN AND JOHANSSON MODEL (WJ) [4]

This is a quadratic model that was derived along a strict formal route from an algebraic form of the Reynolds-stress equations, subject to the weak-equilibrium assumption. Apart from being a low-Re formulation, it differs from the models of Gatski and Speziale [1] and Speziale and Xu [19] in respect of the treatment of the production-to-dissipation ratio P_k/ε. Wallin and Johansson have shown that the non-linear system of equations in the stresses can be solved in the form of a linear system of equations, complemented by a non-linear scalar equation for P_k/ε, whereas other models are based on the assumption that this ratio is given explicitly, allowing the inversion of the implicit algebraic stress equations. The default Wallin and Johansson form uses the k–ω set of equations. Here, in addition to this original version, a variation of the Launder–Sharma form of the ε-equation has also been implemented, after minor adjustments to the damping functions to satisfy grid-turbulence and local-equilibrium constraints.

3.5. THE ABE, JANG AND LESCHZINER MODEL (AJL) [6]

This quadratic low-Re model differs in two important respects from others. First, it augments the basic quadratic constitutive form of (5) by two additive fragments intended to account, respectively, for high normal straining and strong near-wall anisotropy. Second, it uses a form of the ω-equation that is much closer than Wilcox's form to the ε-equation. Specifically, it includes products of k and ω gradients and coefficients for the production and destruction terms which are directly equivalent to normally used in the ε-equation.

An influential additive model fragment accounts specifically for strong near-wall anisotropy and for the correct decay towards two-component turbulence that is observed in DNS. This decay cannot be represented solely by the use of terms combining the strain and vorticity, and there is a need to introduce a tensorially correct term that takes into account the wall orientation. In the present model, the wall-direction indicator is:

$$d_i = \frac{N_i}{\sqrt{N_k N_k}}, \quad N_i = \frac{\partial l_d}{\partial x_i}, \quad l_d = y_n \ (= \text{ wall distance}), \tag{11}$$

which is then used in the wall-anisotropy correction,

$$^w a_{ij} = -f_w \left(d_i d_j - \frac{\delta_{ij}}{3} d_k d_k \right), \tag{12}$$

with f_w being a viscosity-related damping function. In term (12), a composite time-scale is used, which combines the macro-scale k/ε with the Kolmogorov scale
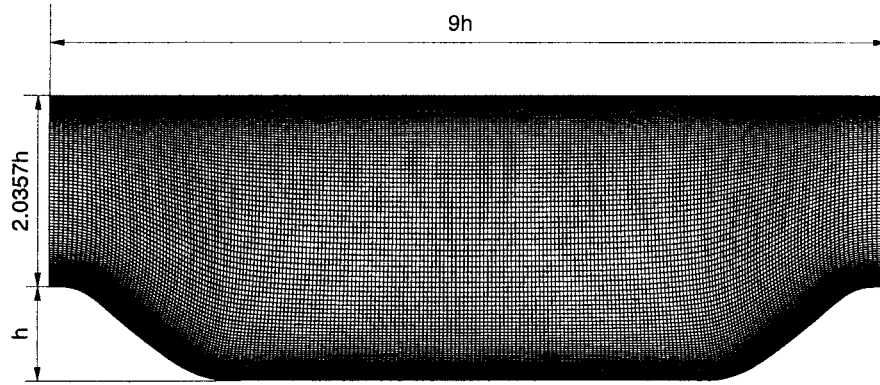
Figure 2. Mesh used for the RANS computations.

$\sqrt{\nu/\varepsilon}$. The damping function f_w then provides a smooth transition between the two scales across the near-wall layer.

4. Numerical Framework

The present RANS calculations were performed with a non-orthogonal, collocated, cell-centered finite-volume approach implemented in the code 'STREAM' [25, 26] and subsequently upgraded by Apsley and Leschziner [11]. Convection of both mean-flow and turbulence quantities is approximated by the 'UMIST' scheme [27] – a second-order TVD approximation of the QUICK scheme of Leonard [28]. Mass conservation is enforced indirectly by way of a pressure-correction algorithm. Within this scheme, the transport and the pressure-correction equations are solved sequentially and iterated to convergence.

The computational domain was covered with a mesh of 228 × 133 nodes, as shown in Figure 2. This was selected on the basis of grid-independence studies, one result of which (with the Launder–Sharma model [18]) is shown in Figure 3. Streamwise periodicy is imposed by forcing the conditions at the inflow and outflow boundaries to be identical. As part of this procedure, the flow rate is dynamically adjusted during the iterative solution so as to adhere to the prescribed Reynolds number. To provide an adequate resolution of the viscous sublayer and the buffer layer adjacent to the solid walls, the minimum wall-normal grid spacing at the wall was maintained at 10^{-3} of the hill height, which corresponds to a wall coordinate y^+ of order 0.1 for low-Re calculations. For the high-Re GS model, the y^+ value, determined with the turbulence energy as the velocity-scale, was maintained above 11.
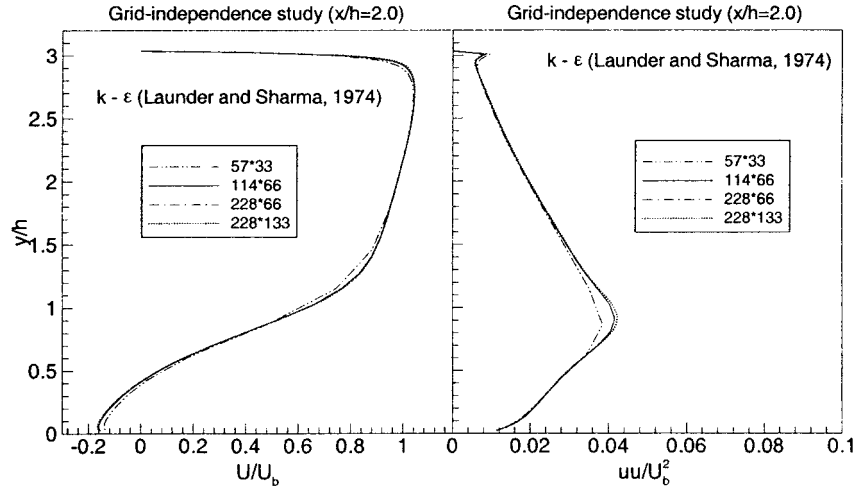
Figure 3. Grid-independence study – velocity and normal-stress profiles at $x/h = 2.0$.

5. RANS-LES Comparisons

This section presents comparisons between model predictions and the LES solution, which contrast the predictive performance of the various models examined. The results relate to both the mean-flow behaviour and the turbulence field, the latter including profiles of stress anisotropy and its invariants and the length-scale derived from the ε- or the ω-equation.

An overall view is conveyed in Figure 4 by way of nine plots of streamfunction contours, one for the LES solution, two relating to the linear baseline EVMs and the remaining six to NLEVMs. It is already at this global level that some substantial differences between different models are observed. This sensitivity to modelling is due, in part, to the streamwise periodicity and the fact that the reattachment point depends strongly on the predicted separation point, the angle of the separation streamline at that point and the behaviour of the model in the immediate vicinity of the reattachment point.

The LES solution gives the reattachment point at $x = 4.7h$. The linear k–ε EVM (LS-ε) returns, much as expected, a premature reattachment at $x = 3.4h$, while the majority of the more elaborate models overestimate the recirculation length, some by a substantial margin, providing a first indication that the level of turbulent mixing predicted by most models in the separated shear layer is too low. There is, furthermore, a general tendency for ω-based models to give a longer recirculation zone than that predicted by ε-based models. This is seen most starkly by comparing the solutions for the linear LS-ε and WX-ω models, as well as those obtained from the two versions of the WJ model. The original WJ-ω version includes a slight variation of Wilcox's low-Re ω-equation, while the other has been obtained upon a replacement of the ω-equation with Launder–Sharma's ε-equation, slightly modified to ensure a compliance of the model with both the decay of grid
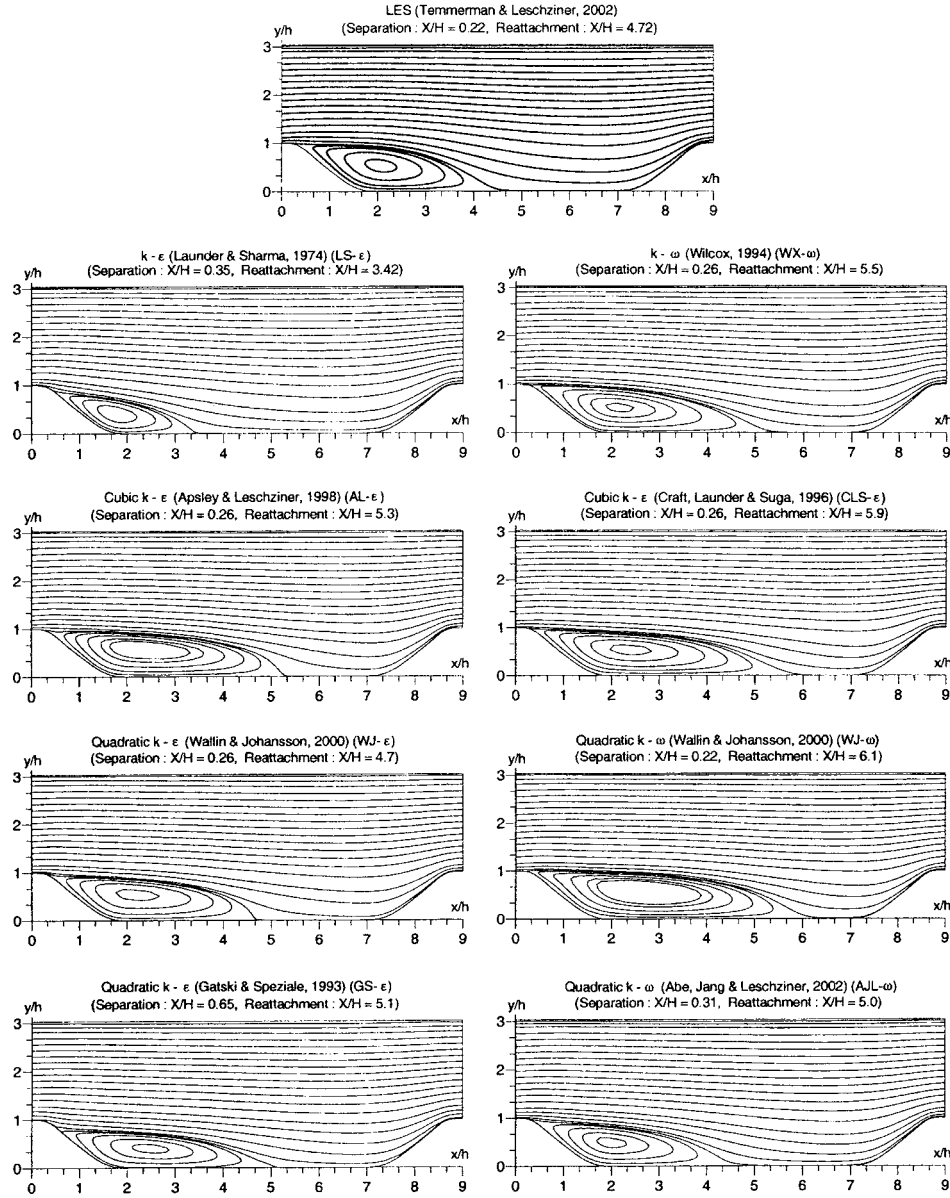
LES (Temmerman & Leschziner, 2002)
(Separation : X/H = 0.22, Reattachment : X/H = 4.72)

k - ε (Launder & Sharma, 1974) (LS- ε)
(Separation : X/H = 0.35, Reattachment : X/H = 3.42)

k - ω (Wilcox, 1994) (WX-ω)
(Separation : X/H = 0.26, Reattachment : X/H = 5.5)

Cubic k - ε (Apsley & Leschziner, 1998) (AL-ε)
(Separation : X/H = 0.26, Reattachment : X/H = 5.3)

Cubic k - ε (Craft, Launder & Suga, 1996) (CLS-ε)
(Separation : X/H = 0.26, Reattachment : X/H = 5.9)

Quadratic k - ε (Wallin & Johansson, 2000) (WJ- ε)
(Separation : X/H = 0.26, Reattachment : X/H = 4.7)

Quadratic k - ω (Wallin & Johansson, 2000) (WJ-ω)
(Separation : X/H = 0.22, Reattachment : X/H = 6.1)

Quadratic k - ε (Gatski & Speziale, 1993) (GS- ε)
(Separation : X/H = 0.65, Reattachment : X/H = 5.1)

Quadratic k - ω (Abe, Jang & Leschziner, 2002) (AJL-ω)
(Separation : X/H = 0.31, Reattachment : X/H = 5.0)

Figure 4. Stream-function contours.

turbulence and the log-law in fully-developed channel flow. It is important to note, however, that the tendency for the ω-equation to return a longer recirculation zone depends greatly on the precise form of the equation. In particular, the equation that is a part of Wilcox's 1994 low-Re model [16] (the one used here and denoted by WX-ω) tends to give much longer separation regions than the earlier 1988 form

[29], although the main difference between the two is the presence or absence of (evidently, highly influential) viscosity-related damping functions, the effects of which extend well beyond the viscous sublayer. Here, the low-Re variant, although linear, already returns an excessively long recirculation zone, while the 1988 model has been found to give a recirculation zone only slightly longer than that resulting from the LS-ε model.

Another observation arising from the solutions presented in Figure 4, as well as others not included herein, is that ω-based models tend to return more acute reattachment streamlines than the ε-based equivalents, which signifies a slower recovery from the reverse flow as reattachment is approached and thus resulting in a downstream shift in the reattachment point. This difference is recognized, for example, when comparing the solutions derived from the two WJ variants. A form of the AL model, not included herein, combines the basic AL formalism with a slight variation of Wilcox's ω-equation, and this gave a reattachment behaviour, relative to the ε-based parent model, consistent with that seen by comparing the two WJ variants. However, there are exceptions to this general trend, as seen by reference to the solutions for the GS-ε and CLS-ε models. Hence, this may not be directly linked to the nature of the length-scale variable chosen, but perhaps rather to the manner in which near-wall processes are modelled, especially in the length-scale equation. The GS-ε form is exceptional in that it predicts a significant delay in separation, probably reflecting errors rooted in the wall-laws. Despite this late separation, reattachment is delayed, and this defect would have been worse had separation been predicted correctly. As will be seen later, this behaviour is associated with far too low levels of shear stress predicted by the GS-ε model in the separated shear layer and beyond. A realizable variant of the GS-ε model, by Rung et al. [4], was also investigated and was found to give a very similar solution; it is not therefore included herein. Based on the general view presented in Figure 4, the models performing best are those of Abe et al. (AJL-ω) and the ε-based form of the Wallin–Johansson model (WJ-ε). However, the latter displays a wrong reattachment behaviour, which contributes, fortuitously, to the accurate prediction of the reattachment point.

Mean-velocity profiles are presented in Figure 5. Results are included for four sections: $x/h = 0.05$, 2, 6 and 8. The first station is of considerable interest here, because it indicates the degree to which the 'inlet' conditions are affected by the inner solution. Normally, the flow at this position is anchored to the prescribed inlet conditions. Here, however, these conditions 'float' and depend on the quality of the solution between the inlet and outlet planes. This first section shows the flow as it approaches the separation point (which is around $x/h = 0.3$). The second is close to the middle of the recirculation zone; the third is downstream of the (LES-predicted) reattachment point; and the forth is in the strongly accelerating region on the hill's windward side. The majority of models are seen to return rather poor representations of the LES solution. Most show common features: a wrong boundary-layer structure ahead of separation (following the strong
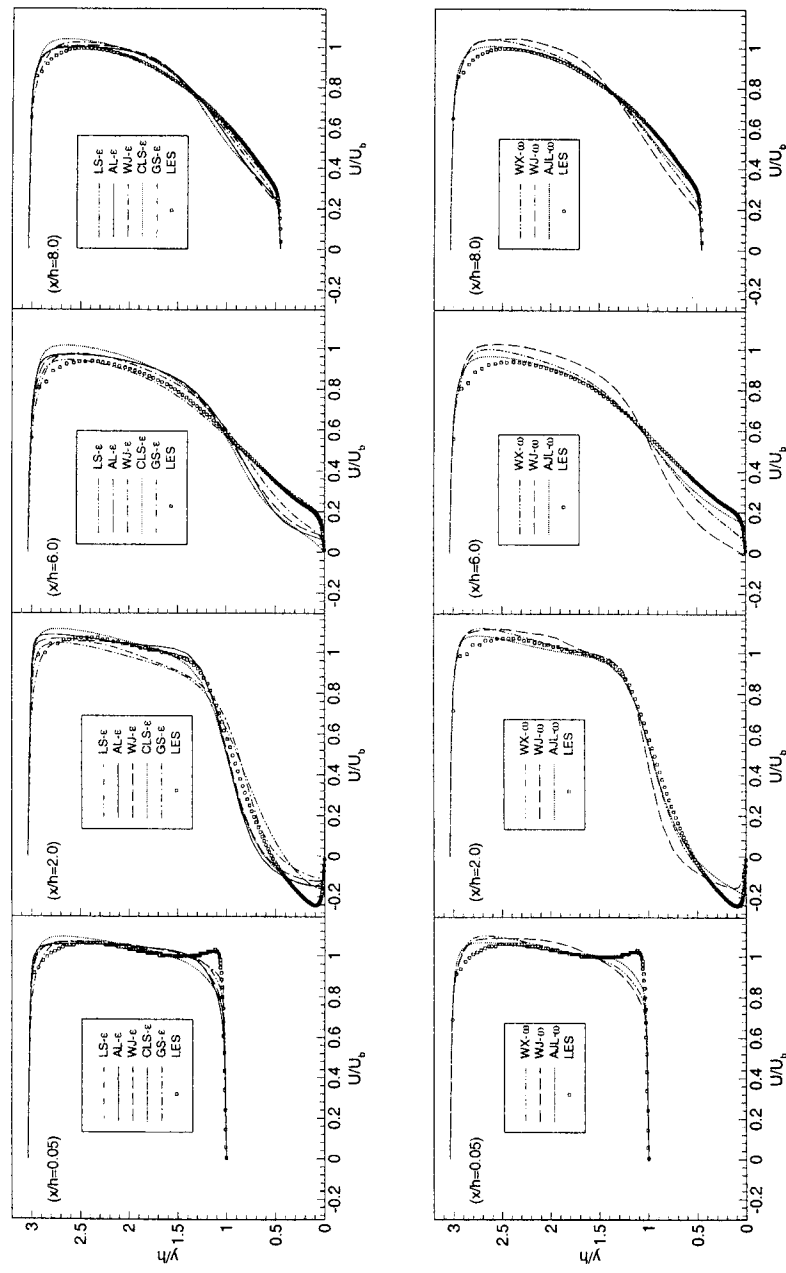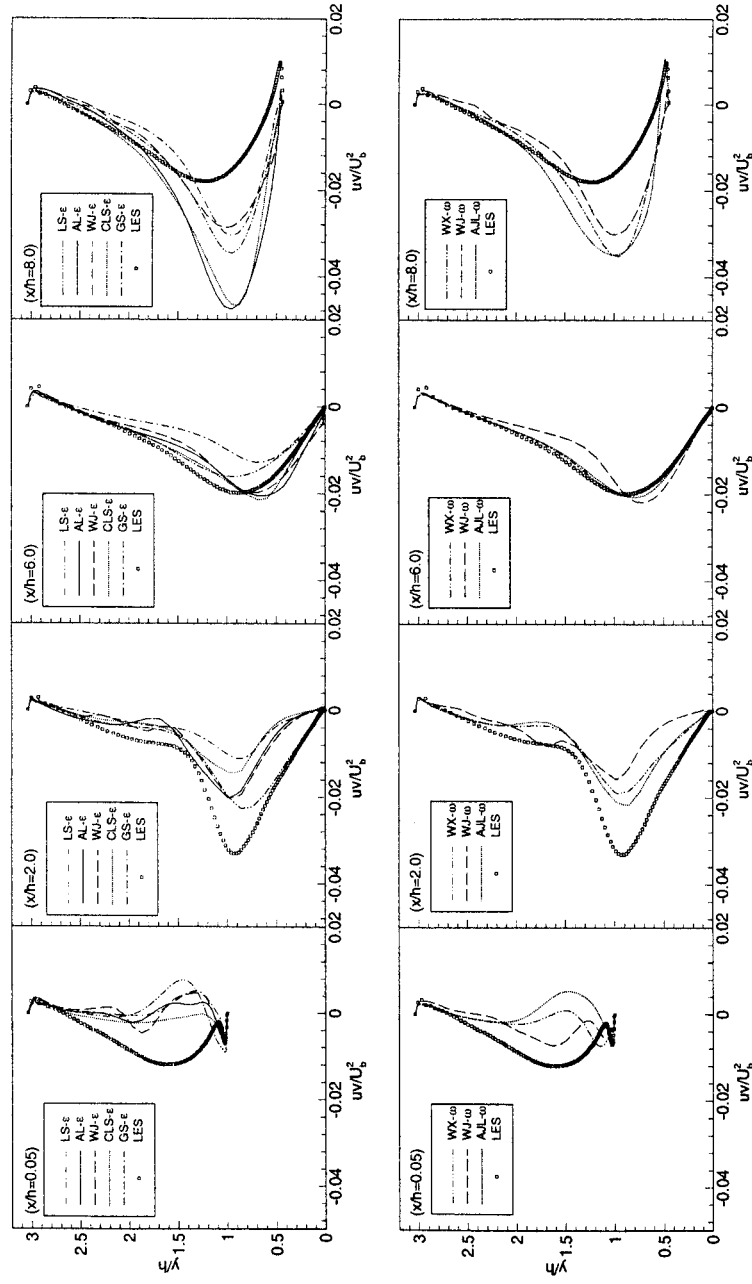
Figure 5. Profiles of streamwise velocity.

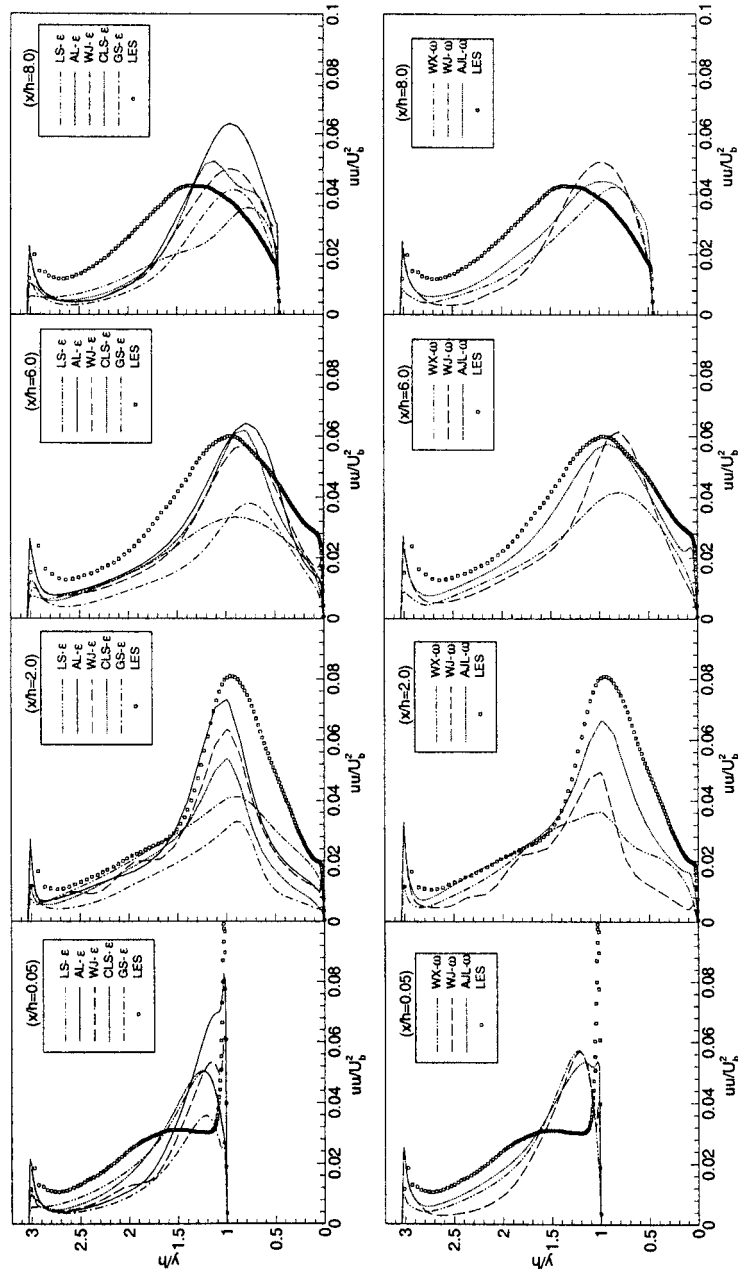*Figure 6.* Profiles of shear stress.
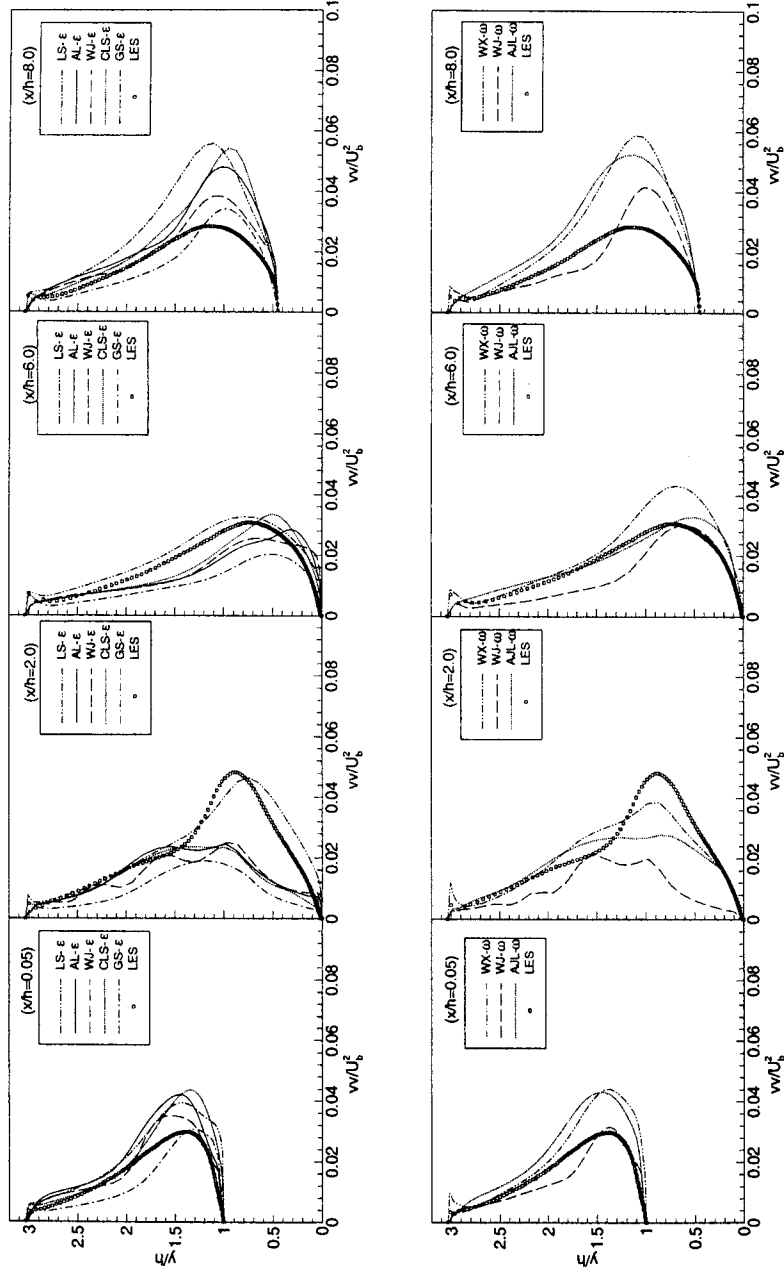
Figure 7. Profiles of streamwise normal stress.

Figure 8. Profiles of transverse normal stress.

upstream acceleration); excessive shear strain in the separated shear layer, coupled with an excessively thick, low-velocity reverse-flow region; and seriously excessive post-reattachment wake defect, due to a delayed reattachment and slow post-reattachment recovery. The linear models aside, the only mild exception to the above behaviour relates to the AJL-ω model. Whilst certainly not providing a faithful representation upstream of the separation point and within the recirculation region, the model gives a more appropriate shear-strain level in the shear layer and a broadly correct post-reattachment behaviour. As regards the linear EVMs, the LS-ε model gives a satisfactory post-reattachment agreement, but this is, fortuitously, a consequence of a far too rapid recovery in the recirculation zone and a premature reattachment. In contrast, the linear WX-ω model performs well in the separated zone, but gives a delayed reattachment and slow post-reattachment recovery. As this model, in common with the LS-ε model, does not resolve anisotropy, does not account for the influence of curvature on turbulence and cannot discriminate between the effects of different types of strain, its favourable mean-flow behaviour cannot be attributed to physically realistic model features.

Shear-stress profiles are given in Figure 6, while normal-stress profiles are included in Figures 7 and 8. The normal stresses are also presented in Figure 9 in the form of profiles for the anisotropy $a_{ij} = \overline{u_i u_j}/k - 2/3\delta_{ij}$ for a sub-set of four models: CLS-ε, AL-ε, WJ-ω and AJL-ω. Profiles of the anisotropy invariants A_2, A_3, and $A \equiv 1 - (9/8)(A_2 - A_3)$ are contained in Figure 10 for the same four models considered in Figure 9. The significance of A is that it varies between '1', for isotropic turbulence, and '0', for two-component turbulence at a wall. The mean-flow behaviour is most strongly linked to the shear-stress level and the pressure gradient, while the normal stresses – although dynamically active – are less influential here, because the velocity over most of the separated shear layer is fairly well aligned with the x-y axes in terms of which the velocity vector and stresses are resolved. The shear-stress profiles at $x = 2h$ (Figure 6), show that all models underestimate the mixing in the separated shear layer, some by a large margin: those models predicting the lowest levels – CLS-ε, WJ-ω give less than 50% of the LES value – tend also to return the longest recirculation zones. The GS-ε model yields especially low values for both the shear and normal stresses, typically only 30–50% of the LES levels. The linear WX-ω model is also seen to give a far too low shear stress, while the AJL-ω model predicts the highest shear stress and a recirculation zone which is only slightly in excess of the LES value.

The fact that none of the models returns a sufficient level of shear stress is curious and points to a failure of all models to resolve some influential mechanism in the shear layer. In their paper focusing on the LES solutions, Temmerman et al. [14] report the observation, derived from visualisations, of a distinctly period motion in the shear layer perhaps associated with post-separation Kelvin–Helmholtz-like instabilities. Another observation is that the separation line moves in time across a substantial proportion of the leeward hill side (approximately within $-0.05 < x/h < 0.7$). Both processes induce large-scale motions which contribute substan-
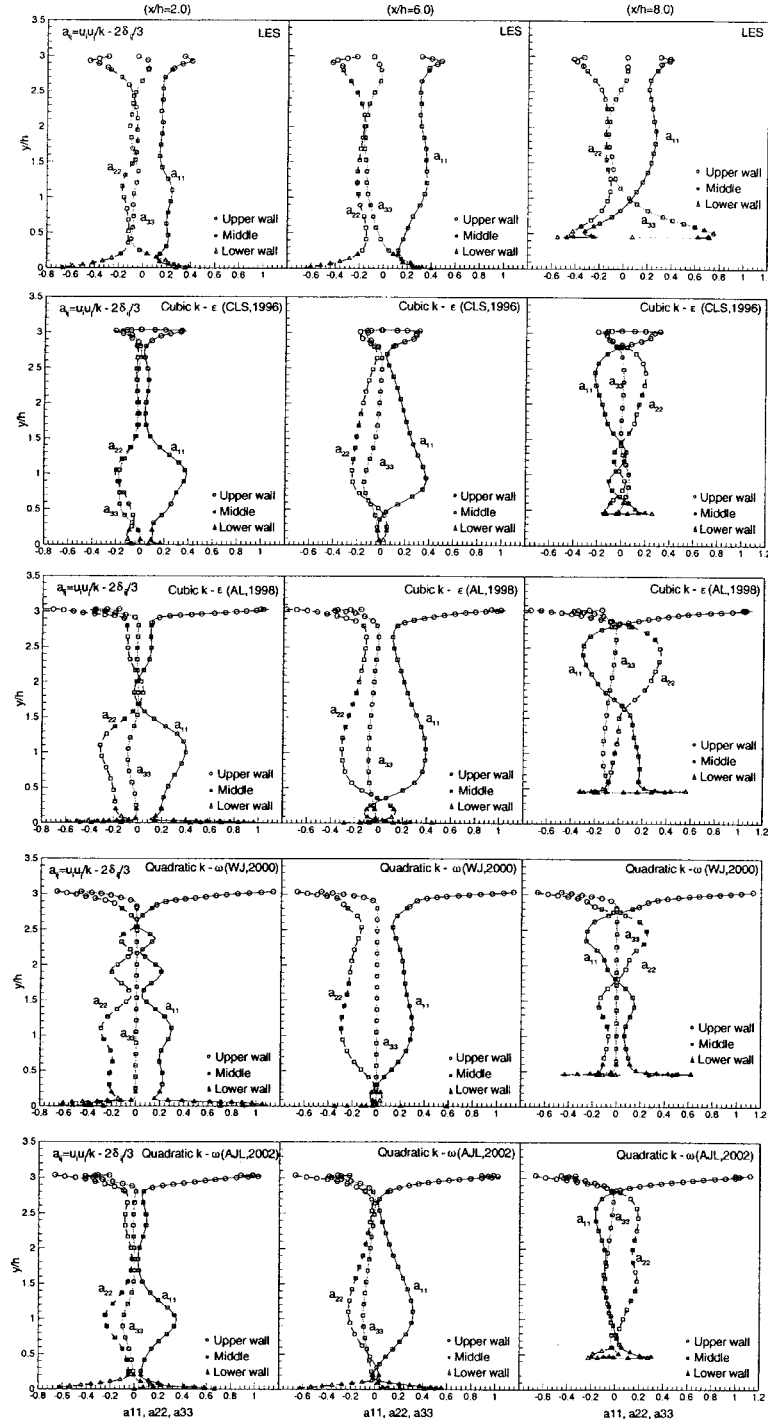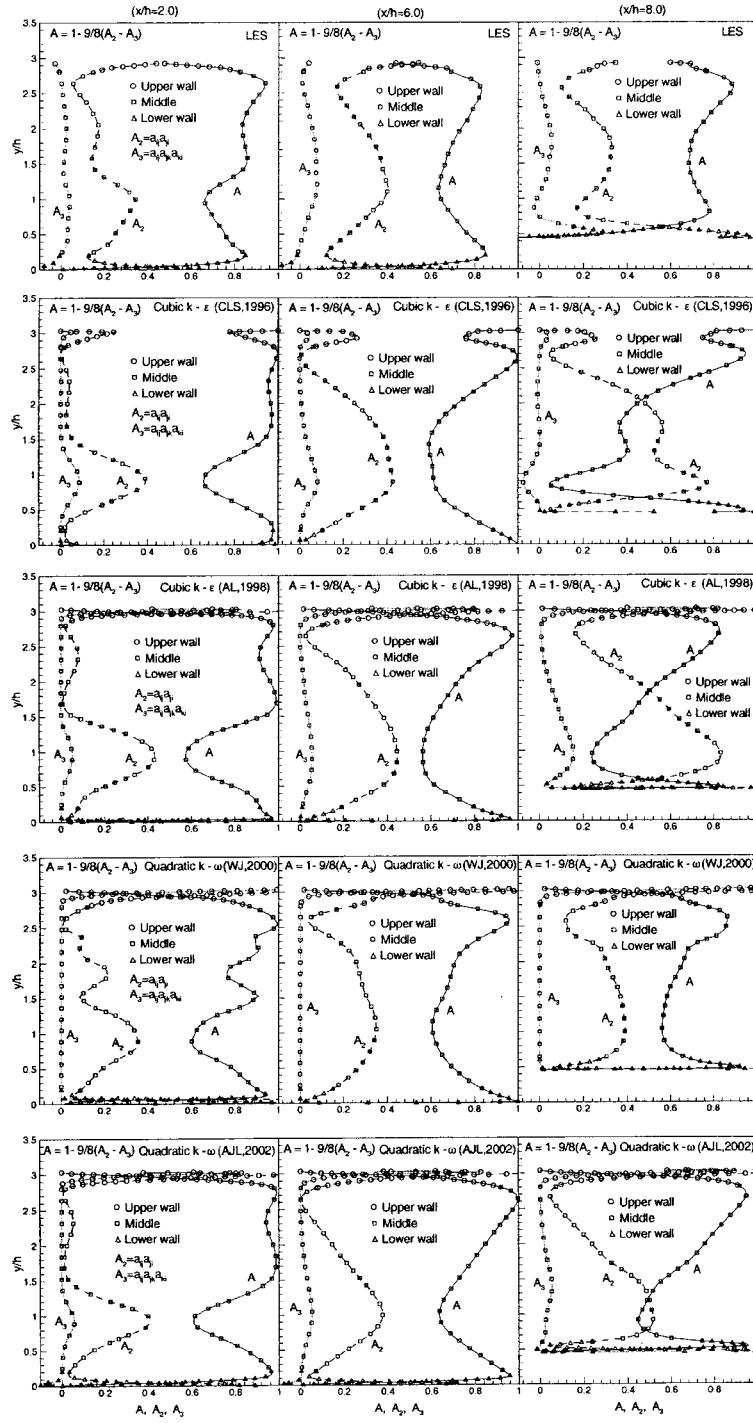
Figure 9. Anisotropy profiles.

Figure 10. Profiles of anisotropy invariants.

tially to the resolved stress, but which are not properly represented by any of the turbulence models. In particular, the strong temporal variation in the separation location results in the presence of large-scale, highly energetic eddies at the time-averaged separation point, while the models link the turbulence state at this point to the much smaller scales embedded in the boundary layer ahead of the separation. For a model to give the correct mean-flow behaviour with the wrong shear stress, that model must give rise to compensating errors, through the pressure gradient and normal stresses. A clear example is the LS-ε model which produces a premature reattachment, yet also gives too low a shear stress in the shear layer.

Figure 6 shows that, ahead of the separation point, all model-predicted shear stresses are very different from the LES solution. It must be noted, however, that the flow at this position has undergone a severe upstream acceleration. The conditions during the acceleration phase are exemplified by the profiles at the location $x/h = 8$. Here, all models seriously over-estimate the shear stress. One reason is an insufficient level of upstream recovery, resulting in an excessive shear strain at around $y/h = 1$. Another likely reason is that shear-stress transport may be influential in the strongly accelerating region. This process is not accounted for in any formal sense in NLEVMs, whilst being approximated in EARSMs by $(\overline{u_i u_j}/k)T_k$, with T_k denoting the turbulence-energy transport. The importance of shear-stress transport is suggested by the observation that full second-moment-closure calculations performed by the Jang and Leschziner and included in an ERCOFTAC workshop compendium of Jakirlic et al. [9] show much improved agreement in respect of the shear stress at $x/h = 8$ and $x/h = 0.05$, despite defects similar to those of NLEVMs in the recirculation zone, the shear layer and the immediate post-reattachment region. With the flow poorly represented at $x/h = 8$, the poor agreement at $x/h = 0.05$ is not surprising.

An interesting feature at $x/h = 8$ is the shear-stress reversal at the wall. This is not associated, as one might suspect at first sight, with the presence of a second recirculation zone nesting on the windward side of the hill – although skin-friction data show that the flow is very close to separation. Rather, the reversal is rooted in the fact that the shear stress considered here is that derived from the x–y-oriented velocity fluctuations, in contrast to the stress that arises from wall-oriented fluctuations. The latter does not reverse, and the reversal of the former is thus a consequence of the rotation of the stress system from the wall-oriented frame of reference to one that is aligned with the x–y system. Any prediction of this reversal thus clearly relies heavily on a correct representation of all near-wall stress components, especially the anisotropy. Only the AJL-ω model resolves this feature unambiguously; there is no more than a hint that the WJ-ε model does so too. At $x/h = 6$, agreement between shear-stress predictions and the corresponding LES distribution is fairly close, although the shear stress returned by all NLEVMs, but the AJL-ω model, is too high close to the wall, while it is too low in the upper portion of the shear layer above $y/h = 0.5$ – a region in which conditions are dictated by those in the separated shear layer upstream. As is seen from Figure 5,

the upper portion of the shear layer at $x/h = 6$ is also characterized by excessive shear strain. This is entirely consistent with the features observed in the shear layer at $x/h = 2$, namely low shear stress and high shear strain. Closer to the wall, an excessive shear stress encourages early reattachment. Thus, those models giving the highest near-wall shear stress, namely AL-ε and WJ-ε, also cause rapid recovery as the reattachment point is approached, a process reflected by the steep angle of the separation streamline at the reattachment point. The third ε-based model, CLS-ε, does not conform to the above description of the near-wall behaviour, but this is likely to be due to the use of the length-scale correction (10), which tends to reduce the near-wall length-scale and hence the viscosity. Of the NLEVMs, the AJL-ω, gives the best agreement with the LES solution in respect of both the shear stress and the velocity profile at $x/h = 6$, and this is linked to the better results it produces further upstream.

The correct resolution of turbulence anisotropy is one of the principal motives for devising and using NLEVMs. Application of Equation (5) to simple shear shows that the level of anisotropy is dictated by the coefficients q_1–q_3, with q_2 playing an especially influential role. It is this that provides a route, either via calibration or through the formal derivation of (5) from a second-moment closure, to modelling the correct level of anisotropy. On the other hand, the shear stress is hardly linked to the anisotropy and is governed mainly by the leading linear term and the curvature-related quasi-cubic fragments associated with γ_1 and γ_2. The importance of resolving anisotropy lies in the fact that the normal stresses are dynamically active in separated flows and thus influence the momentum balance.

The normal-stress profiles, shown in Figures 7 and 8, demonstrate the qualitative ability of the NLEVMs to represent the anisotropic nature of the flow, but the quantitative agreement with the LES solution returned by most models is generally poor. With attention focused on $x = 2h$, the LES solution gives $\overline{u^2}/\overline{v^2}$ ratios of order 1.7. The separation between the normal stresses is dictated, primarily, by the quadratic fragments in the stress/strain-vorticity relations, and these are clearly effective in all NLEVMs. As is seen from Figures 7 and 8, the predicted $\overline{u^2}/\overline{v^2}$ ratio is in the range 1.4–3.5, with all NLEVMs returning far too low wall-normal stress and also too low streamwise stress. The AL-ε, AJL-ω and WJ-ε models give reasonable agreement in respect of the streamwise normal stress, while the WJ-ω, the CLS-ε and especially the GS-ε models yield substantially too low values. These same models also return amongst the lowest shear-stress and transverse normal-stress levels. At $x/h = 6$, agreement with the LES solution is generally better, with the AJL-ω model performing best and the GS-ε model continuing to give the poorest representation. The indifferent-to-poor performance of the GS-ε and WJ-ω models is all the more remarkable as both are derivatives of related Reynolds-stress closures, and this implies that no particular predictive merits are derived from simplifications of such closures. Indeed, computations with full second-moment models performed by the present authors show that these tend to underestimate the stresses even more seriously than the NLEVMs included in Figures 6–8 (see

[9]). Consistent with earlier observations on the shear stress, the normal stresses at $x/h = 0.05$ and 8 are poorly resolved, and this is again associated with the strong acceleration upstream of $x/h = 8$. A feature deserved to be highlighted is the extremely high near-wall streamwise stress at $x/h = 0.05$. This feature is well resolved only by the AL-ε model. It will be recalled that this model is calibrated so as to allow it to return a broadly correct representation of the near-wall anisotropy, an issue that will be revisited below.

In comparing model-predicted profiles of anisotropy and their invariants A_2, A_3 and $A \equiv 1 - (9/8)(A_2 - A_3)$ to corresponding LES results in Figures 9 and 10, respectively, it must be noted first that the LES data are unreliable close to the upper wall. This has already been pointed out in Section 2 in which it is explained that the grid is too coarse at the upper wall to properly resolve the semi-viscous layer, necessitating the use of an approximate wall law. The departure from reality is indicated by the fact that A fails to approach zero at that wall – a value of zero signifying two-component turbulence – and that a_{22} does not approach -0.66. With attention confined to the 90% reach above the lower wall, it is seen that none of the models represents the LES data more than qualitatively correctly. All return the basic feature of $a_{11} > a_{22}$ in most parts of the flow well away from the wall at $x/h = 2$ and 6. Most models also return a_{33} values slightly below zero, while the WJ-ω model, by virtue of its formulation, gives $a_{33} = 0$, except in the immediate proximity of the wall. At the wall, all models but the AJL-ω and, to a lesser extent, the AL-ε formulations provide a poor description of the anisotropy, and this reflects the fact that the inertial processes affecting the near-wall anisotropy (i.e. those associated with blocking) cannot be described simply by the use of the strain and vorticity terms. Very close to the wall, in the semi-viscous regime, an appropriate calibration based on DNS data can procure a broadly correct asymptotic behaviour. This is the case with the AL-ε and WJ-ω models, which yield $A = 0$ at the wall and which, as shown in Figure 7, are able to resolve the peak streamwise normal stress at $x/h = 0.05$. However, this calibration does not allow the correct behaviour above the viscous near-wall layer to be procured. The CLS-ε model fails to represent any aspect of the near-wall anisotropy, while the AJL-ω model, by virtue of incorporating wall-orientation indicators, reproduces reasonably well the near-wall anisotropy. Figure 11 provides a comparison of model-predicted $A_2 - A_3$ loci in Lumley's realizability map for the AJL-ω, CLS-ε and WJ-ω models, against the LES data, along the lines $x/h = 2, 6$ and 8. In all plots, the open triangular symbols relate to the 5% layer closest to the lower wall, the open circles to the 5% layer closest to the upper wall and the squares to the 90% in the middle. It must be reiterated here that the simulation is not able to return the correct asymptotic behaviour at the upper wall; hence, the parts of the loci identified by the circles in the uppermost three plots in Figure 11 do not represent the real behaviour. Figure 11 demonstrates that the AJL-ω model returns, in contrast to the other two, lower-wall loci that approach the two-component state, identified by $A = 1 - (9/8)(A_2 - A_3) = 0$, broadly along the line representing axisymmetric-contraction strain, in fair accord
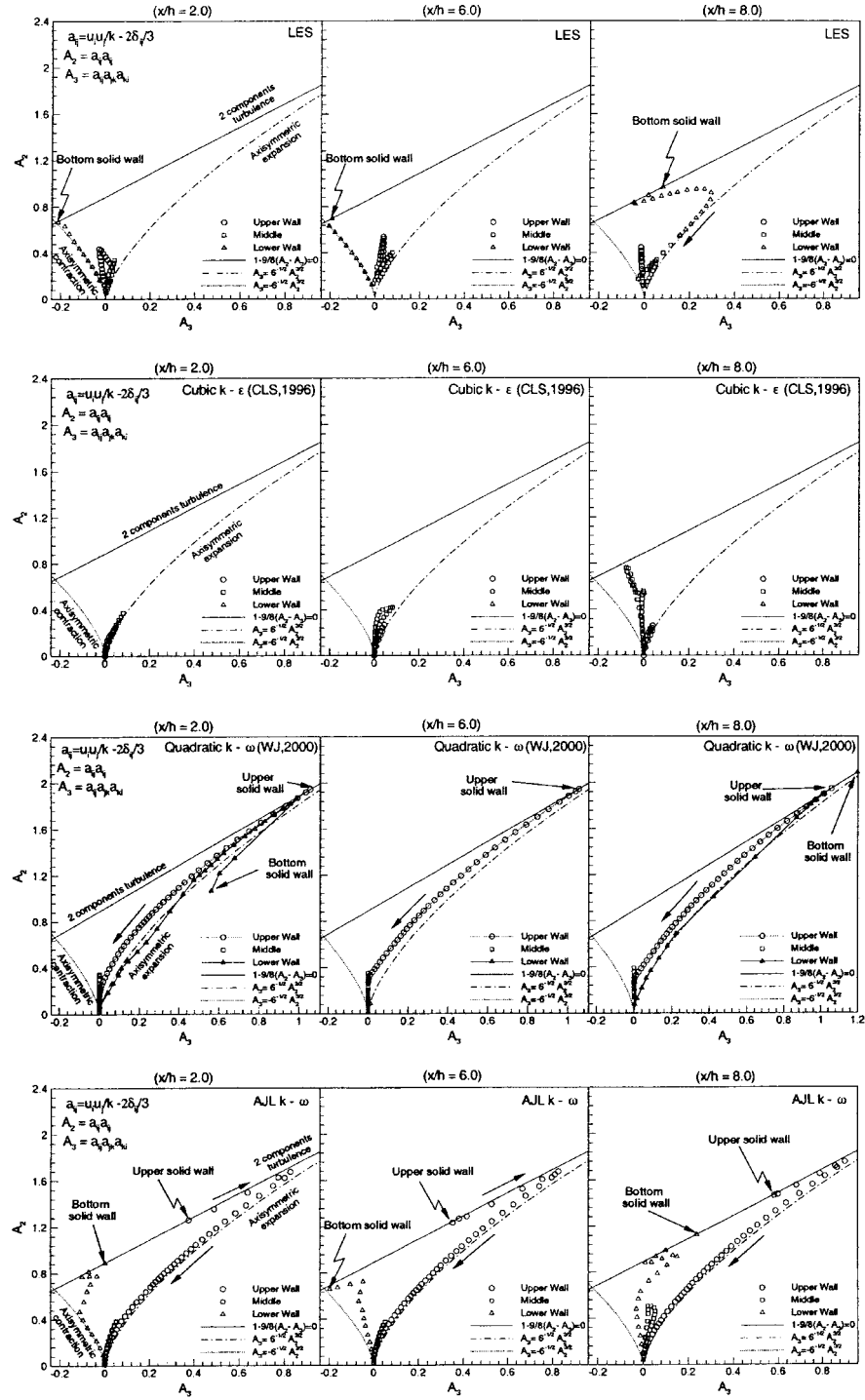
Figure 11. Realizability maps.

with the LES solution. In fact, this is the only model among all those examined which does so. Furthermore, this is the only model which returns a behaviour at the upper wall that is observed in DNS for fully-developed channel flow. At $x/h = 8$, where the flow is accelerating strongly, all models fail to give a realistic description of the stress field, although the AJL-ω still provides a credible $A_2 - A_3$ locus. An interesting feature observed in the simulation is the presence of a very high spanwise intensity at the lower wall, reflected by a steep rise in a_{33} at the expense of a_{11}. This feature is entirely missed by all models, as is the fact that a_{11} remains above a_{22} across the whole flow. To a first approximation, the conditions in the central region around $y/h = 2$–2.5 are akin to those of homogeneous plane strain or axisymmetric contraction. In such circumstances, a_{11} is expected to drop, while a_{22} expected to rise. This is what the models appear to reproduce. While there is an indication in the LES distributions that the separation between the two normal stresses is decreasing during the acceleration process, this decrease, if present, is much weaker than that modelled. The variations returned by the models for A, A_2 and A_3 are all qualitatively correct, the third invariant being very low. However, the general trend of the invariants is strongly influenced by the shear stress, so that fairly large differences between models in respect of the anisotropy components they predict will not be reflected by corresponding differences in the invariants.

As the length-scale equation is a highly influential model component, in addition to the constitutive stress-strain relation, it is of interest to examine the predicted length-scale $L = k^{1/5}/\varepsilon$ relative to the LES data. Unfortunately, a comparison with the LES data involves considerable uncertainty. The grid resolution in the simulation is far from sufficient to extract the dissipation rate directly from its exact definition, and the dissipation was therefore obtained as a balance of all other processes that are associated with the large-scale motion. With this noted, attention is directed to Figure 12, which gives comparisons between model predictions and the LES data. Also included are the lines $L = 2.5y$, which represent the variation consistent with local equilibrium. The figure shows that all models return broadly similar distributions of length-scale, although there are some important differences in detail. Of particular interest in the behaviour at the lower wall, where, surprisingly, the LES solution gives higher length-scale values than do the models. Less surprising is the fact that virtually none of the distributions complies with $L = 2.5y$, reflecting a strong departure from equilibrium in the recirculation region and close to the reattachment point. The models that produce relatively low levels of near-wall length-scale are also those predicting relatively long recirculation zones. This is especially evident when comparing the WJ-ε and WJ-ω models, the latter using Wilcox's ω-equation and giving the lowest near-wall length-scale as well as the longest recirculation zone. The AJL-ω model, using an ω-equation closer to the ε-form, gives a higher length-scale and shorter recirculation zone. The CLS-ε formulation was earlier noted to display an exceptional reattachment behaviour, relative to other ε-based models, predicting one of the longest recirculation zones and a shallow reattachment angle more typical of that
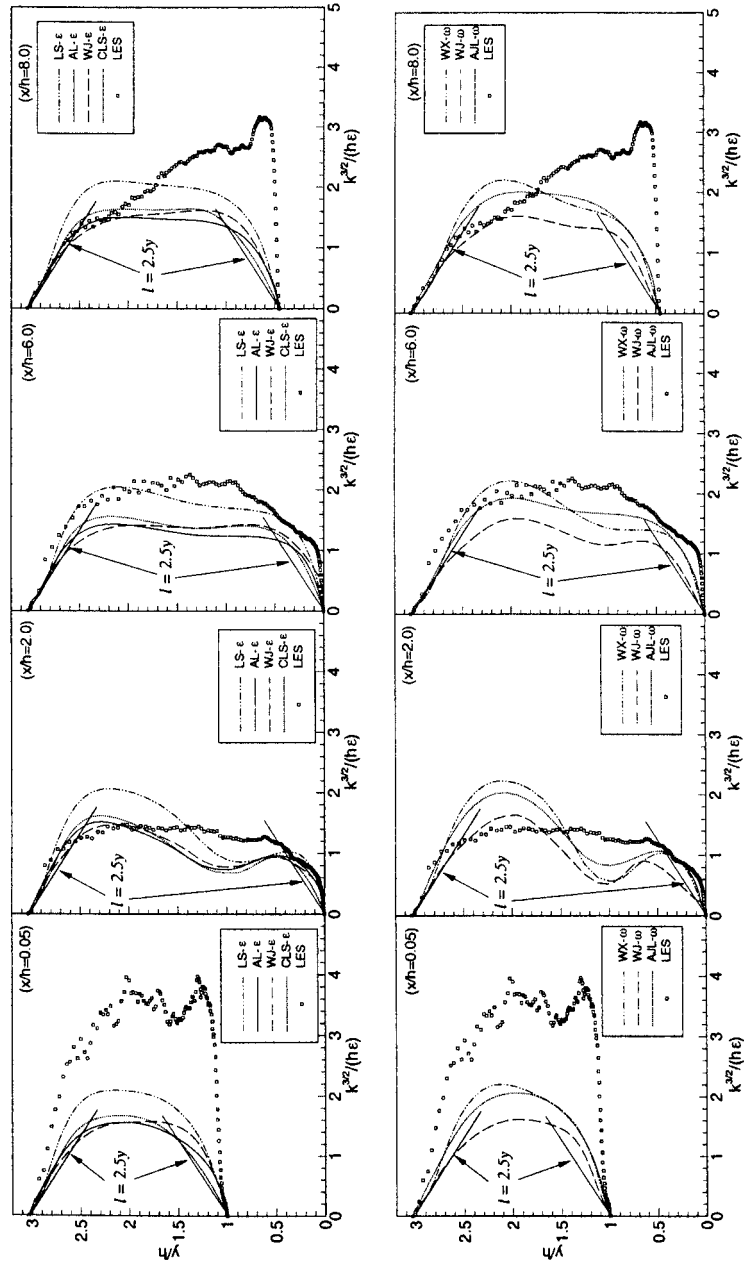
Figure 12. Profiles of macro length-scale.

returned by ω-based models. Consistently, the near-wall length-scale it predicts is close to that produced by ω-based models, a behaviour associated with the use of the correction (10). Among all the models examined, the linear LS-ε form gives the largest length-scale across virtually the entire flow and, consistently, the shortest separation region.

It is difficult to judge whether the large discrepancies observed at $x/h = 0.05$ and 8 reflect genuine model defects. It was shown earlier that the models seriously misrepresent the anisotropy and grossly over-estimate the shear stress in the acceleration phase. In part, this is attributable to the omission of stress transport or its approximation by way of the turbulence-energy transport. In addition, the plots for the anisotropy a_{ij} show that the acceleration and curvature on the hill's windward side cause a drastic redistribution of turbulence energy near the wall from the streamwise and cross-stream normal stresses to the spanwise component, a process which is not captured even qualitatively by any of the models. Based purely on arguments of turbulence generation and on the observed variations of stresses and strains around $y/h = 1$–1.5 at $x/h = 8$, it is possible to infer that the models should tend to produce a higher level of k than that of the simulation. It is indeed observed that the modelled k at $x/h = 0.05$ and 8 is higher than that simulated over about 40% of the lateral extent of the flow adjacent to the lower wall. However, the excess is not dramatic. In contrast, the simulated rate of dissipation is much smaller than that modelled (by up to a factor of 4), and it is this which is mainly responsible for the differences seen in Figure 12. Beyond $y/h = 2$, both the modelled and simulated dissipation-rate levels are low, and slight differences in this variable translate to the large differences in the length-scale observed in Figure 12. The implication of the behaviour close to the lower wall, where the modelled dissipation is much higher than the simulated level, is that the discrepancies observed in Figure 12 in this region may reflect a fundamental defect of all length-scale equations in strong acceleration, perhaps linked to a misrepresentation of the generation and destruction of the dissipation rate in terms of those of the turbulence energy.

6. *A-Priori* Analysis

The advantage of well-resolved simulation data, in contrast to experimental data, is that the former essentially offer a complete description of the flow evolution and can, therefore, be post-processed to yield whole-field distributions of most statistical correlations of interest. Such distributions may then be used for calibrating and/or *a-priori* testing of model fragments. In the case of LES data, some limitations are imposed by the imperfect resolution. This applies, in particular, to correlations of small-scale fluctuations, notably those contributing to the dissipation rate.

When attention focuses on Reynolds-stress models, all terms but stress dissipation in the exact second-moment-transport equations are dominated by large-scale

turbulent motions and can be extracted with fair accuracy. The dissipation can then be obtained as an imbalance of all other terms contributing to the budget. The above range and detail of data allow the realism of closure proposals to be assessed in some depth.

In the case of non-linear eddy-viscosity models, the stresses are linked to the mean-velocity field by the constitutive equations (5), and the scope for *a-priori* testing is more limited. What can be done, however, is to insert the LES mean-flow fields into (5), as well as into the associated transport equations, and then examine the stresses, the fragments of (5) and the turbulence energy that are returned by the model in comparison with the corresponding LES data. Clearly, differences between corresponding data for any one quantity are responsible for 'driving' the modelled mean flow (that which arises from a full RANS solution) away from the simulated solution. Model improvements must strive to minimize the differences, and this is the ultimate purpose of performing the *a-priori* analysis. The distributions for the stresses, the fragments of (5), etc., that arise from the full RANS solutions can also be compared with the corresponding data derived from the *a-priori* evaluation, and this can give additional information of which model elements respond especially sensitively to changes in the mean flow, thus identifying these elements as requiring special attention.

The result of the above process is given in Figures 13–16 for four models: the linear WX-ω model and the non-linear WJ-ω, AJL-ω and AL-ε models. Figure 13 gives, on the left, distributions of the deviatoric component of the streamwise normal stress $(\overline{u^2} - (2/3)k)/U_b^2$ and the total stress $\overline{u^2}$ for the locations $x = 2h$ (upper row) and $6h$ (lower row). For each variable, the symbols denote the *a-priori* analysis, while the corresponding lines come from the complete (*a-posteriori*) RANS calculation. The line formed with the symbol '**L**' denotes the solution derived directly from the LES. The adjacent central plot gives *a-priori* and *a-posteriori* results for the *linear fragment* of the deviatoric normal-stress component, again compared with the actual LES solution. As the WX-ω model is linear, there is only one term in the stress-strain relation, and the distribution in the central plot are, therefore, identical to those on the left-most plot, which shows the total deviatoric stress $(\overline{u^2} - (2/3)k)/U_b^2$. Finally, the right-hand side plots show corresponding *a-priori* and *a-posteriori* distributions for the shear stress.

Figure 13 reveals immediately that the WX-ω model returns an entirely wrong representation of the streamwise normal stress. The deviatotic part is not simply of the wrong magnitude, but also of the wrong sign at $x/h = 2$. This applies to both the *a-priori* and the actual computed result. A similar behaviour is observed with any other linear EVM. Also, the shear stress at $x/h = 2$ is much too low, and it is this which encourages a delayed reattachment which then gives, fortuitously, fair agreement in respect of the mean flow. The fact that the predicted mean flow is quite close to the LES field is implied by the relatively small differences between the *a-priori* and *a-posteriori* distributions, but clearly this is due to wrong reasons. At $x/h = 6$, the *a-priori* shear stress is significantly lower than that predicted
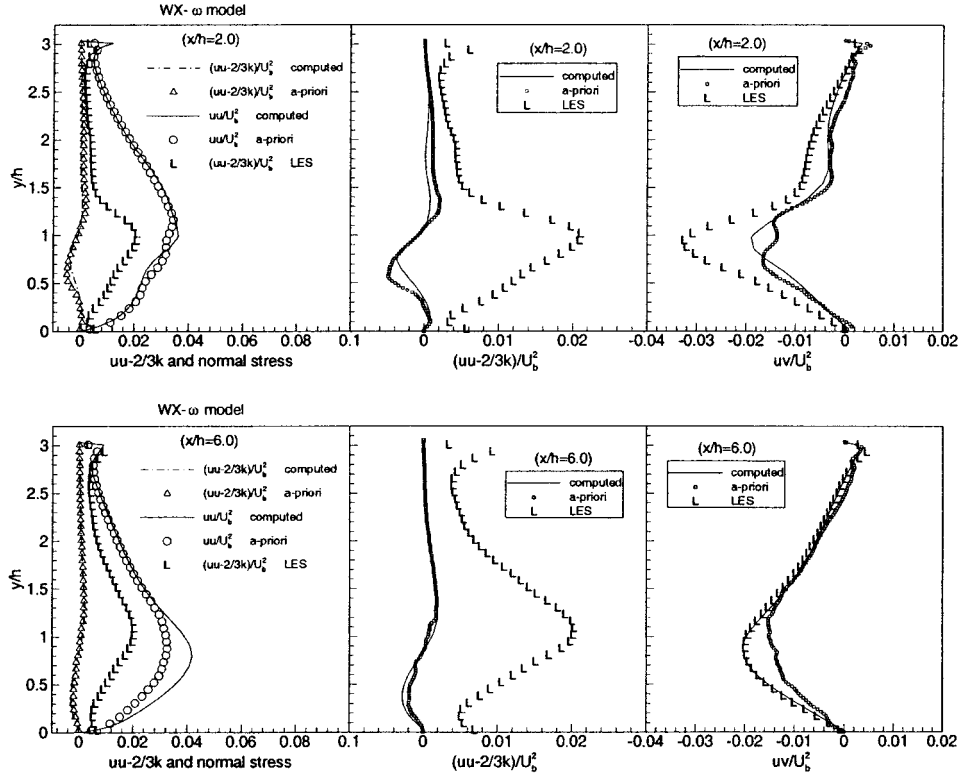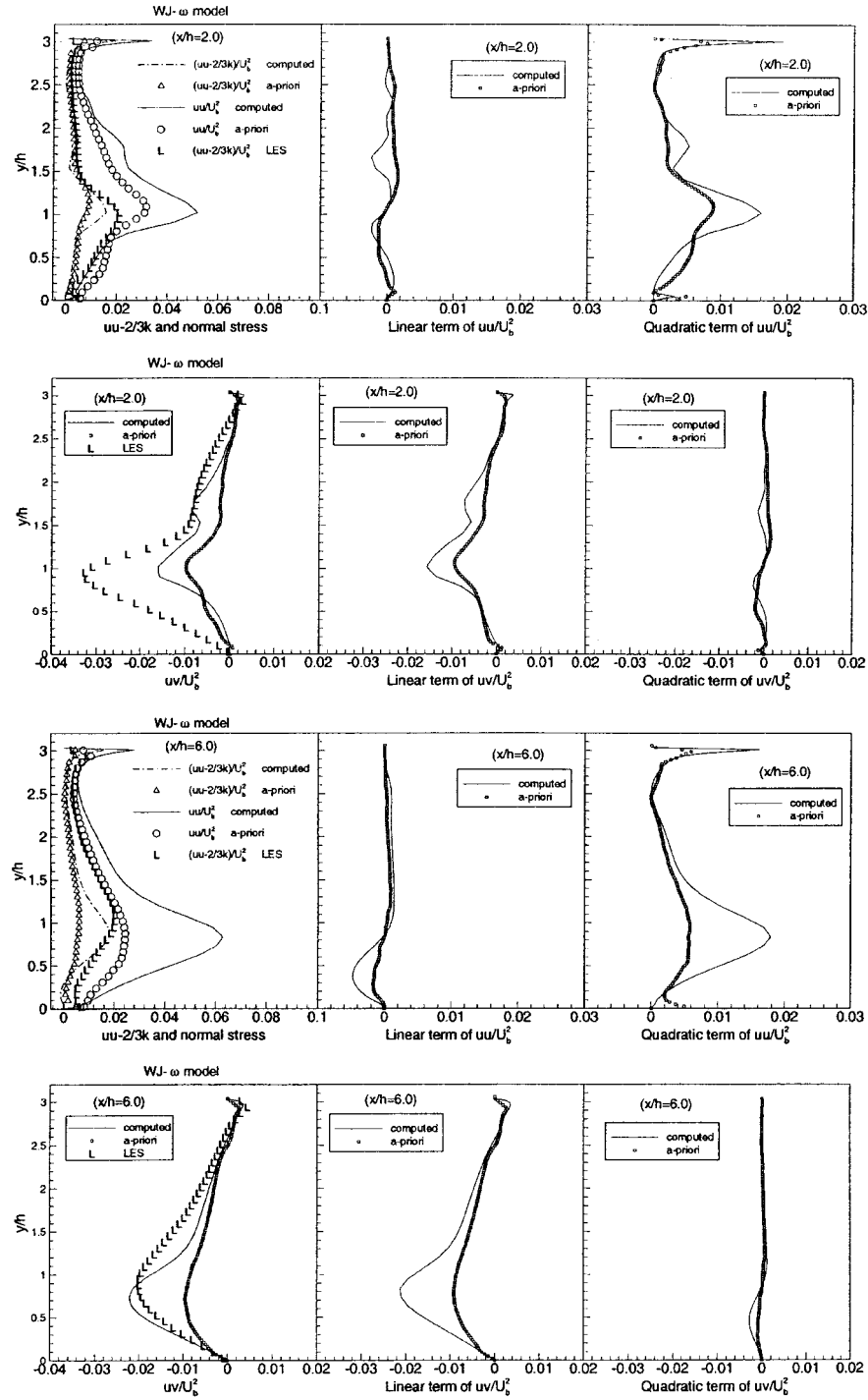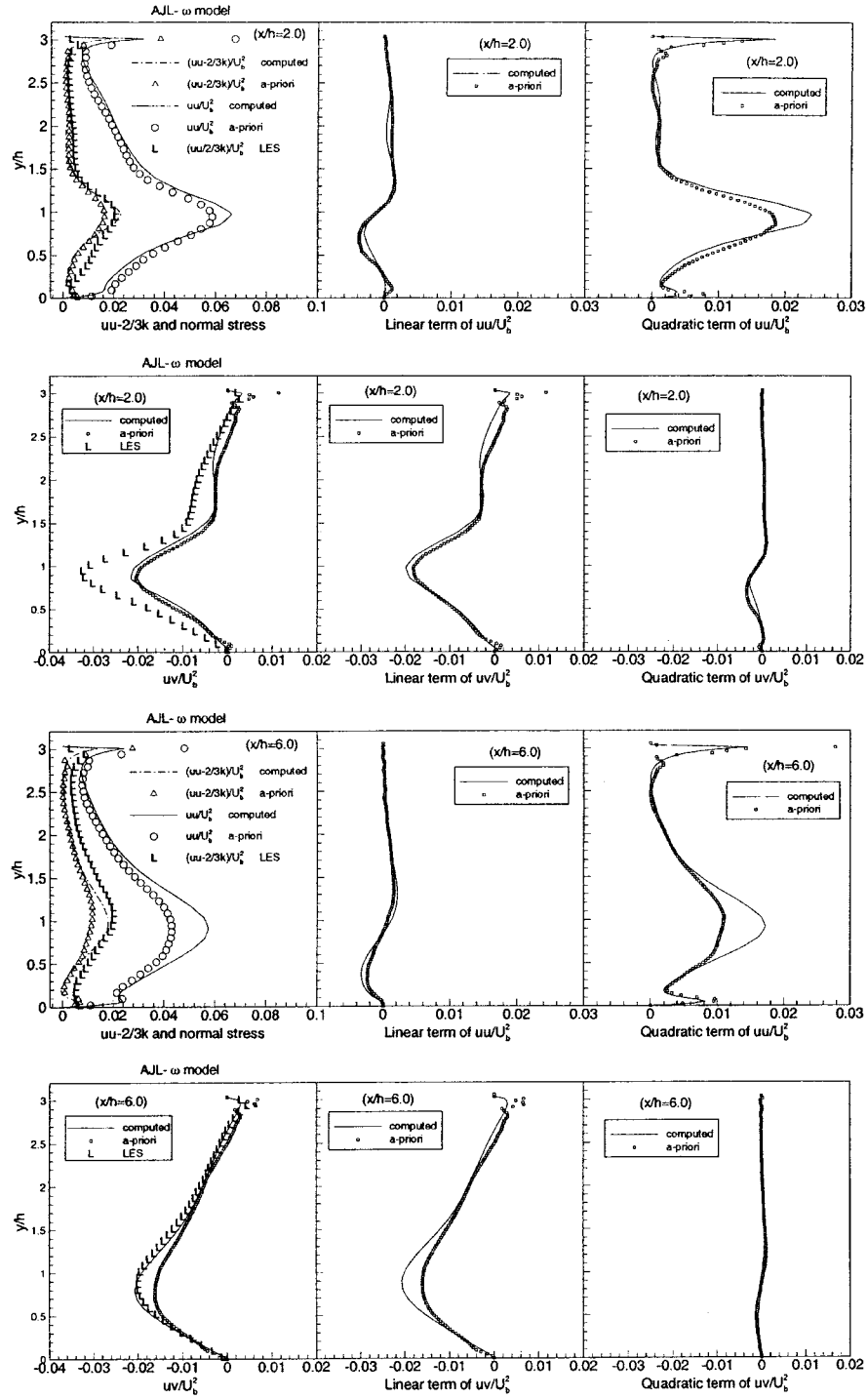
Figure 13. A-priori analysis, WX-ω model.

by the model in the full calculation. The model elevates the stress, to agree well with the LES distribution, by virtue of the fact that the full calculation steepens the shear strain at $x/h = 6$ beyond the level it should have and thus increases the shear stress; again, this is an advantageous effect, but is due to the wrong reasons.

Comparisons for the quadratic WJ-ω and the AJL-ω models are provided in Figures 14 and 15, respectively. In every horizontal set of three plots, the middle plot relates to the linear contribution in Equation (5), while the right-most plot relates to the quadratic fragment. It is noted first, in relation to the shear stress, that the WJ-ω model returns an exceptionally low *a-priori* value and substantial discrepancies between the *a-priori* and the *a-posteriori* distributions, the latter being shifted towards the LES distribution. This shift, indicative of model defects, is caused by an increase in the shear strain and an adjustment of the velocity field to give a significant (and wrong) elongation of the recirculation zone. As the shear stress is dictated, principally, by the linear term, the defect lies in that term being evidently too small.

The contrast of the results from the AJL-ω model to those of the WJ-ω formulation is striking. The former gives much higher levels of shear stress and a

Figure 14. A-priori analysis, WJ-ω model.

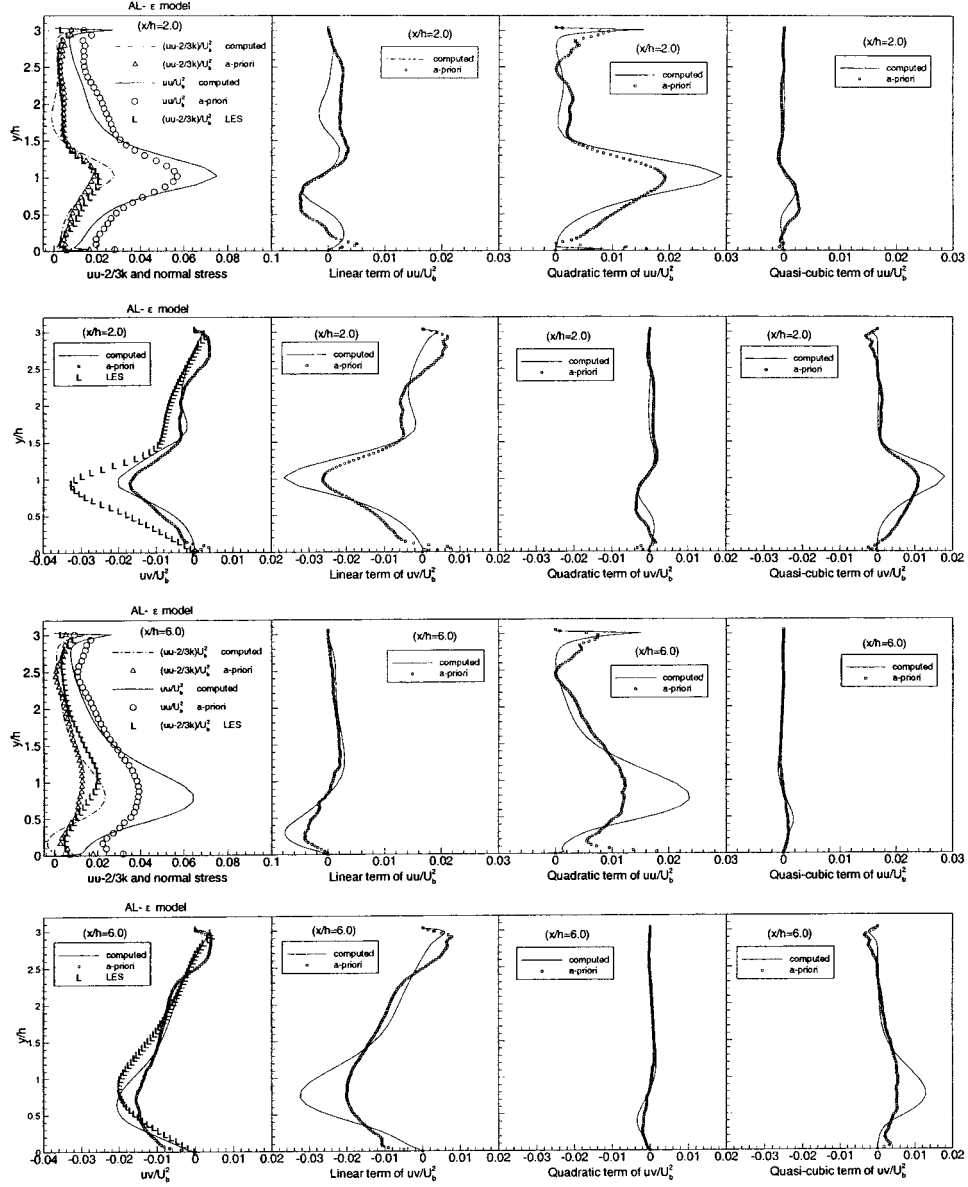*Figure 15. A-priori* analysis, AJL-ω model.

Figure 16. A-priori analysis, AL-ε model.

fairly close correspondence between the *a-priori* and the *a-posteriori* distributions, especially at $x/h = 2$, signifying a broadly correct velocity field. Here too, the shear stress is evidently dictated by the linear term, although the quadratic term makes a non-negligible contribution. The linear term is here seen to give, correctly, a much higher contribution than the corresponding term in the WJ-ω model. The fact that the shear stress at $x/h = 2$ is still too low, relative to the LES distribu-

tion, provides added support to the view, expressed earlier, that the LES-computed separated shear layer is affected by an organized motion associated with vortices induced by Kelvin–Helmholz instability. At $x/h = 6$, the solution returned by the AJL-ω model is still clearly superior to that derived from the WJ-ω form, although there is evidently a slight adjustment to the velocity field, resulting in a shift of the shear stress towards the LES distribution. At this location, any effects arising from the organized motion of the shear layer are likely to be insignificant.

The normal-stress distributions confirm the clear superiority of the AJL-ω model. Consistently, the WJ-ω model gives an insufficient level of normal stress and large differences between the *a-priori* and *a-posteriori* distributions. Here, the quadratic term exerts a decisive influence, correcting the entirely wrong stress-strain linkage provided through the linear term. The WJ-ω model yields a seriously insufficient quadratic contribution, however, which produces an *a-priori* normal stress far below the LES level. An improvement in the level of agreement arises in the full solution, but this is, as noted already, at the expense of an inappropriate adjustment to the velocity field. It may be supposed that the poor performance of the WJ-ω form is rooted, principally, in the ω-equation, rather than in the non-linear stress-strain/vorticity relation. However, a corresponding *a-priori* analysis for the WJ-ε variant (not included) gave only slightly better results, and this suggests that the defects are mainly due to model components other than the length-scale equation.

Results are finally presented for the AL-ε model in Figure 16. Although this model is also quadratic in 2D flow, it is formulated to include separate quasi-cubic contributions associated with γ_1 and γ_2 in Equation (5) and representative of streamline curvature. For this reason, the contribution of these terms is displayed separately in the right-most plots of Figure 16. As seen from the shear-stress-related distributions, this model also predicts a substantially too low shear stress at $x/h = 2$. As is the case with the WJ-ω model, the *a-priori* levels are well below those which the full solution returns, and this leads to an increase in the shear strain within the shear layer and to an inappropriate elongation of the recirculation zone. Responsibility for this behaviour appears to lie with the quasi-cubic terms, which depress the shear stress by virtue of curvature. Hence, the implication is that an improvement in the model would be achieved by a reduction of this contribution. A comparison between the corresponding *a-priori* distributions returned by the AJL-ω and the AL-ε models for $x/h = 6$ reinforce the conclusion that the quasi-cubic terms have a detrimental effect on the model's performance. The linear and quadratic contributions are similar, while the quasi-cubic contribution tends to depress the shear stress, which is undesirable. In the actual solution, the adjustment of the velocity field strengthens the cubic contribution further, which is then associated with a compensating steep increase in the linear contribution.

As regards the normal stress, the quadratic fragment is, again, of decisive influence. At $x/h = 2$, the sum of the *a-priori* distributions for the linear and quasi-cubic terms is very similar to the linear contribution of the AJL-ω model.

Moreover, the profiles of the respective quadratic terms are very similar. Hence, the implication is that the model should perform reasonably well in respect of the streamwise anisotropy. The fact that the full solution returns an excessive value in the shear layer is linked to the disadvantageous effect of the quasi-cubic terms on the shear stress. It is this component that needs to be addressed to improve the model's performance. The arguments presented above are also consistent with the behaviour observed at $x/h = 6$.

7. Conclusions

An investigation has been presented of the performance of several non-linear eddy-viscosity models when applied to a separated flow in a periodically-constricted channel for which highly-resolved LES data are available. The emphasis has been on the predictive quality of the models and on understanding the origin of defects associated either with the non-linear constitutive equation for the stresses or the length-scale equation.

The initial comparisons of (*a-posteriori*) model predictions with the LES data have illustrated the high level of sensitivity of the solutions to relatively minor variations in modelling details. The expected poor performance of the linear k–ε model has been confirmed. While the basic linear k–ω form of Wilcox has returned much better results for the mean flow, it has been shown that this favourable behaviour is due to wrong reasons, in particular a serious under-estimation of the shear stress in the separated shear layer. This points to the outstanding importance of the precise form of the length-scale-governing equation, including the particular constants and viscosity-related damping functions used. A judiciously chosen form of the equation can compensate, phenomenologically, for defects in other parts of the model, but the compensation is not general and restricted to mean-flow properties. The comparisons also show that the linear models give an entirely wrong deviatoric streamwise normal stresses, not only in terms of magnitude, but also in terms of sign.

Most non-linear eddy-viscosity models, whether operating with ε- or ω-based length-scale equations, have been found to over-estimate the extent of the separation zone. One reason is the seriously insufficient shear stress returned in the separated shear layer. The origin of this defect varies from model to model, as is demonstrated by the *a-priori* analysis. For example, in the case of the 'cubic' Apsley–Leschziner (AL-ε) model, the quasi-cubic fragments associated with curvature cause an undesirable depression in the shear stress. In contrast, the Wallin–Johansson (WJ-ω) model suffers from a combination of insufficient linear contribution and wrong length-scale field predicted by the Wilcox form of the ω-equation which is a component of this model. Use of the ε-equation shortens the recirculation zone, but this is a consequence of a rapid near-wall recovery just upstream of the reattachment point, associated with an excessive length-scale value. This is one particular ailment from which the ω-equation does not seem to suffer.

A reduction in the near-wall length-scale by a Yap-type correction term, as is done in the Craft–Launder–Suga (CLS-ε) model, results in a more realistic reattachment behaviour, similar to that of ω-based models, but then leads to a further delay in the reattachment and a worsening of the mean-flow prediction.

To derive advantages from non-linear modeling, the non-linear constitutive equation needs to be carefully coupled with a length-scale equation that combines the favourable characteristics of the ε-equation away from the wall with those of the ω-equation close to the wall. This is realized by the Abe–Jang–Leschziner model (AJL-ω), which also contains new wall-anisotropy and high-normal-strain model fragments. The *a-priori* analysis for this model indicates that both the linear and quadratic contributions to the constitutive stress-strain relation perform adequately, giving a mean flow that agrees well with the LES solution.

All non-linear models capture qualitative aspects of the anisotropy, but the quantitative representation is poor. Particular problems arise in the strongly accelerating region upstream of the hill crest, where stress transport is influential and where the LES solution shows turbulence energy to undergo a curious redistribution process near the wall, which cannot be captured even qualitatively by any of the models. Most models do not represent the near-wall anisotropy correctly and do not return the appropriate asymptotic behaviour associated with wall blocking. An exception is the Abe et al. model (AJL-ω), which contains tensorial wall-orientation terms that ensure the correct near-wall behaviour. The advantages of this feature has been clearly demonstrated by way of anisotropy profiles.

Of the models examined, that by Abe et al. exhibits, overall, the best behaviour: it returns a broadly correct mean-flow field, gives the best (though by no means perfect) agreement in respect of the shear stress and reproduces best the near-wall anisotropy. This favourable performance is consistent with the *a-priori* analysis, which gives *a-priori* distributions for both shear and streamwise normal stresses that are close to corresponding distributions arising from the complete model solution. The Wallin-Johansson model, although derived formally from the Reynolds-stress equations, performs rather poorly in the present flow. To a degree, this is consonant with the authors' experience, not verified herein, that Reynolds-stress models also tend to give far too low levels of shear-stress in the separated shear layer and hence an excessively long separation zone.

Appendix A: Turbulence-Model Constants, Coefficients and Functions

Table I. Coefficients in non-linear stress/strain-vorticity relations (note additional definitions following tables).

Model	C_μ	(q_1, q_2, q_3)	$(\gamma_1, \gamma_2, \gamma_3, \gamma_4)$
Gatski & Speziale, (GS)	$\dfrac{1}{2}\alpha_1 C_1^*$	$(\alpha_3 C_3^*,\ \alpha_2 C_2^*,\ 0)$	$(0, 0, 0, 0)$
Craft, Suga & Launder (CLS)	$\dfrac{0.3(1-e^{-0.36\exp(0.75\max(\bar s,\bar w))})}{1+0.35\left((\max(\bar s,\bar w))\right)^{3/2}}f_\mu$ $\bar s=\sqrt{2s_{ij}s_{ij}},\ \bar w=\sqrt{2w_{ij}w_{ij}}$	$C_\mu f_\mu(-0.4,\ 0.4,\ -1.04)$	$C_\mu^3 f_\mu(40,\ 40,\ 0,\ -80)$
Apsley & Leschziner (AL)	$\dfrac{(-a_{12}^*)}{1+\overline{\xi}^2/3-\overline{\psi}^2}\dfrac{f_P}{\sigma^*}f_\mu$ $\overline{\xi}=0.222,\quad \overline{\psi}=0.623$	$\left(\dfrac{f_P}{\sigma^*}\right)^2\left(6(a_{11}^*+a_{22}^*),\ a_{11}^*-a_{22}^*,\ 0\right)$	$4C_\mu(\dfrac{f_P}{\sigma^*})^2(\dfrac{1}{3}\overline{\xi}^2,\overline{\psi}^2,\dfrac{3}{2}\overline{\psi}^2,\dfrac{3}{2}\overline{\xi}\psi)$
Wallin & Johansson (WJ)	$-\dfrac{1}{2}\beta_1 f_\mu$	$(1-f_\mu^2)\dfrac{3B_2-4}{\max(S_2,II_s^{eq})},$ $-\{f_\mu^2\beta_4-(1-f_\mu^2)\dfrac{B_2}{2\max(S_2,II_2^{eq})}\},$ 0	$(0, 0, 0, 0)$
Abe, Jang & Leschziner (AJL)	$C_B C_\mu^* f_\mu$ $C_\mu^*=0.12$	$4C_D C_B\left(C_\mu^* f_\mu\right)^2\left(1-f_w(A)\big|_{A=26}\right),$ $4C_D C_B\left(C_\mu^* f_\mu\right)^2\left(1-f_w(A)\big|_{A=26}\right),$ 0	$(0, 0, 0, 0)$

Table II. Coefficients in k and ε equations (note additional definitions following tables).

Model	$C_{\varepsilon 1}$	$C_{\varepsilon 2}$	σ_k	σ_ε	S_ε
Launder & Sharma (LS-ε)	1.44	1.92	1.0	1.3	0
Gatski and Speziale (GS-ε)	1.44	1.83	1.0	1.3	0
Craft, Suga & Launder (CLS-ε)	1.44	1.92	1.0	1.3	YAP (eq. (10))
Apsley and Leschziner (AL-ε)	1.44	1.83	$\dfrac{1.0}{1+\overline{\xi}^2/3-\overline{\psi}^2}$	$\dfrac{1.37}{1+\overline{\xi}^2/3-\overline{\psi}^2}$	0
Wallin & Johansson (WJ-ε)	1.44	1.92	1.0	1.3	0

Table III. Coefficients and functions in k–ω models (note additional definitions following tables).

	α^*	β^*	α	β	σ_k	σ_ω	S_l
Wilcox (1994) (WX-ω)	$\dfrac{\frac{1}{40}+\frac{Re_{t\omega}}{R_k}}{1+\frac{Re_{t\omega}}{R_k}}$ $R_k=6.0$	$\dfrac{9}{100}\dfrac{\frac{5}{18}+\left(\frac{Re_{t\omega}}{R_\beta}\right)^4}{1+\left(\frac{Re_{t\omega}}{R_\beta}\right)^4}$ $R_\beta=8.0$	$\dfrac{5}{9}\dfrac{\frac{1}{10}+\frac{Re_{t\omega}}{R_\omega}}{1+\frac{Re_{t\omega}}{R_\omega}}$ $R_w=2.7$	$\dfrac{3}{40}$	2	2	0
Wallin & Johansson (WJ-ω)	C_μ/β^*	As WX-ω but with $R_\beta=10.0$	As WX-ω	$\dfrac{3}{40}$	2	2	0
Abe, Jang & Leschziner (AJL-ω)	$C_\mu^* f_\mu/\beta^*$	$\dfrac{9}{100}\dfrac{\left(\frac{\beta}{3\beta_0}\right)+\left(\frac{Re_{t\omega}}{R_\beta}\right)^4}{1+\left(\frac{Re_{t\omega}}{R_\beta}\right)^4}$ $R_\beta=9.0$ $\beta_0=0.09$	$0.45\alpha^*$	0.0747	$\dfrac{1.2}{f_t}$	$\dfrac{1.5}{f_t}$	E_ω

Table IV. Coefficients and functions in k–ε models.

	f_μ	D	f_1	f_2	S_ε
Launder & Sharma (LS-ε)	$\exp\left(\dfrac{-3.4}{(1+R_t/50)^2}\right)$	$2\nu\left(\dfrac{\partial k^{1/2}}{\partial x_i}\right)^2$	1	$1-0.3e^{-R_t^2}$	$2\nu\nu_t\left(\dfrac{\partial^2 U_i}{\partial x_j \partial x_k}\right)^2$
Wallin & Johansson (WJ-ε)	$1-\exp\left(-\dfrac{2.4\sqrt{y_n^*}+0.003(y_n^*)^2}{26}\right)$	$2\nu\left(\dfrac{\partial k^{1/2}}{\partial x_i}\right)^2\exp(-0.7y_n^*)$	1	$1-0.3e^{-R_t^2}$	$2\nu\nu_t\left(\dfrac{\partial^2 U_i}{\partial x_j \partial x_k}\right)^2$
Craft, Suga & Launder (CLS-ε)	$1-\exp[-(R_t/90)^{1/2}-(R_t/400)^2]$	$2\nu\left(\dfrac{\partial k^{1/2}}{\partial x_i}\right)^2$	1	$1-0.3e^{-R_t^2}$	$0.0022\dfrac{\bar{s}\nu_t k^2}{\varepsilon}\left(\dfrac{\partial^2 U_i}{\partial x_j \partial x_k}\right)^2$ $(R_t \le 250)$
Apsley & Leschziner (AL-ε)	1	0	1	1	$C_{\varepsilon 2}\dfrac{\varepsilon^{(1)}\varepsilon}{k}e^{-0.0038(y_n^*)^2}$

Notes:

- The turbulent Reynolds numbers and related non-dimensional wall distances are:

$$R_t = \frac{k^2}{\nu\varepsilon}, \quad R_{t\omega} = \frac{k}{\nu\omega}, \tag{A1}$$

$$y_n^* = \frac{y_n k^{1/2}}{\nu}, \quad \hat{y_n} = \frac{y_n (\nu \varepsilon)^{1/4}}{\nu}. \tag{A2}$$

- In the *Gatski and Speziale model*, $C_1^* - C_3^*$ are shear-dependent terms based on the regularisation of the 2D solution [19]

$$C_1^* = \frac{(1 + 2\zeta^2)(1 + 6\zeta^5) + \frac{5}{3}\eta^2}{(1 + 2\zeta^2)(1 + 2\zeta^2 + \eta^2 + 6b_1\eta^6)},$$

$$C_{2,3}^* = \frac{(1 + 2\zeta^2)(1 + \eta^4) + \frac{2}{3}\eta^2}{(1 + 2\zeta^2)(1 + 2\zeta^2 + b_{2,3}\eta^6)}, \tag{A3}$$

where

$$(b_1, b_2, b_3) = (7.0, 6.3, 4.0),$$

$$\eta = \frac{1}{2}\frac{\alpha_3}{\alpha_1}(s_2)^{1/2}, \quad \zeta = \frac{\alpha_2}{\alpha_1}(-w_2)^{1/2},$$

$$s_2 = \{\mathbf{s}^2\}, \quad w_2 = \{\mathbf{w}^2\},$$

$$\alpha_1 = \left(\frac{4}{3} - C_2\right)g, \quad \alpha_2 = \frac{1}{2}\alpha_1(2 - C_4)g, \quad \alpha_3 = \alpha_1(2 - C_3)g,$$

$$g = \frac{1}{\frac{1}{2}C_1 + \left(\frac{P}{\varepsilon}\right)_{eq} - 1}, \quad \left(\frac{P}{\varepsilon}\right)_{eq} = \frac{C_{\varepsilon 2} - 1}{C_{\varepsilon 1} - 1}$$

and

$$C_1 = 6.8, \quad C_2 = 0.36, \quad C_3 = 1.25, \quad C_4 = 0.40$$

originate from the Speziale et al. [23] pressure-strain model.

- In the *Apsley and Leschziner model* $a_{\alpha\beta}^*$ and σ^* arise from calibration by reference to DNS data for plane channel flow

$$a_{11}^* = 1 + 0.42 \exp(0.296(y_n^*)^{1/2} - 0.040 y_n^*) - \frac{2}{3},$$

$$a_{22}^* = 0.404[1 - \exp(-0.001 y_n^* - 0.000147(y_n^*)^2)] - \frac{2}{3},$$

$$a_{12}^* = -0.3[1 - \exp(-0.00443(y_n^*)^{1/2} - 0.0189 y_n^*)],$$

$$\sigma^* = 3.33[1 - \exp(-0.45 y_n^*)][1 + 0.277(y_n^*)^{3/2} \exp(-0.088 y_n^*)]. \tag{A4}$$

The *non-equilibrium parameter* f_P which accounts for departures of the shear parameter $\sigma = (k/\varepsilon)\sqrt{(\partial U_i/\partial x_j)^2} = (s_2 - w_2)^{1/2}$ from the calibration value σ^* is given by

$$f_P = \frac{2f_0}{1 + \sqrt{1 + 4f_0(f_0 - 1)(\sigma/\sigma^*)^2}}, \tag{A5}$$

where

$$f_0 = 1 + 1.25\max(0.09\sigma^{*2}, 1.0).$$

The additional term in the dissipation equation is based upon a curve fit to the DNS data for the dissipation length:

$$\varepsilon^{(1)} = \frac{C_\mu^{3/4}k^{3/2}}{l_\varepsilon^{(1)}},$$

$$l_\varepsilon^{(1)} = 0.179y\left(1 + \frac{128}{y_n^*}\right)[1 - \exp(-n^{*2}/279)]. \tag{A6}$$

- In the *Wallin and Johansson model*, the following relations arise from the underlying second-moment closure assumption from which the model is derived:

$$\beta_1 = -\frac{6}{5}\frac{N}{N^2 - 2w_2},$$

$$\beta_4 = -\frac{6}{5}\frac{1}{N^2 - 2w_2}, \tag{A7}$$

where

$$N = \frac{c_1'}{3} + (P_1 + \sqrt{P_2})^{1/3} + \text{sign}(P_1 - \sqrt{P_2})\left|P_1 - \sqrt{P_2}\right|^{1/3}, \quad P_2 \geq 0,$$

$$N = \frac{c_1'}{3} + 2(P_1^2 - P_2)^{1/6}\cos\left[\frac{1}{3}\arccos\left(\frac{P_1}{\sqrt{P_1^2 - P_2}}\right)\right], \quad P_2 < 0,$$

$$P_1 = \left(\frac{1}{27}c_1'^2 + \frac{9}{20}s_2 - \frac{2}{3}w_2\right)c_1',$$

$$P_2 = P_1^2 - \left(\frac{1}{9}c_1'^2 + \frac{9}{10}s_2 + \frac{2}{3}w_2\right)^3,$$

$$c_1' = \frac{9}{4}(c_1 - 1), \quad c_1 = 1.8, \quad B_2 = 1.8, \quad II_S^{\text{eq}} = 5.74.$$

- In the Abe, Jang and Leschziner model, the basic constitutive relation (5) is augmented with the two additive fragments

$$
\mathbf{a}^{(s)} = \{1 - f_w(A)|_{A=26}\}\left\{ -2f_{s1}C_B C_\mu^* f_\mu s_{ij} \right.
$$

$$
\left. + 4f_{s2}C_D C_B (C_\mu^* f_\mu)^2 \left(s_{ik}s_{kj} - \frac{\delta_{ij}}{3}s_{mn}s_{mn} \right) \right\}, \tag{A8}
$$

$$
\mathbf{a}^{(w)} = f_w(A)|_{A=26}\left[-\alpha_w \left(d_i d_j - \frac{\delta_{ij}}{3}d_k d_k \right) + 2(1 - f_{r1}^2) \right.
$$

$$
\times \left\{ -\frac{\beta_w C_w}{1 + C_w\sqrt{s_2^* w_2^*}}(s_{ik}^* w_{kj}^* - w_{ik}^* s_{kj}^*) \right.
$$

$$
\left. \left. + \frac{\gamma_w C_w}{1 + C_w s_2^*}\left(s_{ik}^* s_{kj}^* - \frac{\delta_{ij}}{3}s_2^* \right) \right\} \right], \tag{A9}
$$

the former designed to improve the response to strong normal straining and the latter to capture correctly the approach to two-component turbulence at walls. In the above,

$$
f_{s1} = f_{r1}f_{r2}C_{s1}\left(C_D C_\mu^* f_\mu \right)^2 (w_2 - s_2),
$$

$$
f_{s2} = -f_{r1}f_{r2}\left\{ 1 + C_{s2}\frac{C_D C_\mu^* f_\mu}{\sqrt{2}}(\overline{w} - \overline{s}) \right\},
$$

$$
f_{r1} = \frac{w^2 - s^2}{w^2 + s^2}, \qquad f_{r2} = \frac{s^2}{w^2 + s^2},
$$

$$
f_w(A) = \exp\left\{ -\left(\frac{\hat{y}_n}{A} \right)^2 \right\}, \qquad \hat{y}_n = \frac{y_n(\nu\varepsilon)^{1/4}}{\nu},
$$

$$
C_D = 0.8, \quad C_{s1} = 0.15C_\eta, \quad C_{s2} = 0.07C_\eta,
$$

$$
s_{ij}^* = \frac{1}{2}\tau_D\left(\frac{\partial U_i}{\partial x_j} + \frac{\partial U_j}{\partial x_i} - \frac{2}{3}\frac{\partial U_k}{\partial x_k}\delta_{ij} \right), \quad w_{ij}^* = \frac{1}{2}\tau_D\left(\frac{\partial U_i}{\partial x_j} - \frac{\partial U_j}{\partial x_i} \right),
$$

$$
s_2^* = s_{ij}^* s_{ij}^*, \quad w_2^* = w_{ij}^* w_{ij}^*,
$$

$$
\tau_D = \{1 - f_w(A)|_{A=15}\}\frac{k}{\varepsilon} + f_w(A)|_{A=15}\sqrt{\frac{\nu}{\varepsilon}},
$$

$$
\alpha_w = 1, \quad \beta_w = 1/4, \quad \gamma_w = 1.5, \quad C_w = 0.5,
$$

and

$$d_i = \frac{N_i}{\sqrt{N_k N_k}}, \quad N_i = \frac{\partial y_n}{\partial x_i} \tag{A10}$$

represent the orientation of the wall to which the distance y_n relates.

Although this model uses the ω-equation, a number of features of the equation derive from the ε-equation. Thus,

$$\nu_t = C_\mu^* f_\mu \frac{k^2}{\varepsilon} = C_\mu^* f_\mu \frac{k^2}{\beta^* \omega k} = \left(\frac{C_\mu^* f_\mu}{\beta^*}\right) \frac{k}{\omega} = \alpha^* \frac{k}{\omega}, \tag{A11}$$

where

$$f_\mu = \left[1 + \frac{35}{R_t^{3/4}} \exp\left\{-\left(\frac{R_t}{30}\right)^{3/4}\right\}\right] \{1 - f_w(A)|_{A=26}\}.$$

Additional terms and functions arising in the ω-equation are

$$f_t = 1 + 5.0 f_w(A)|_{A=5}, \tag{A12}$$

$$E_\omega = \{1 - f_w(A)|_{A=600}\} C_{\omega 1} C_\mu^* f_\mu \tau \frac{\partial k}{\partial x_j} \frac{\partial \omega}{\partial x_j}, \tag{A13}$$

with $C_{\omega 1} = 1.5$.

Finally, the linear term in (5) contains the coefficient

$$C_B = \frac{1}{1 + \left(C_D C_\mu^* f_\mu\right)^2 \left\{\frac{22}{3} w_2 + \frac{2}{3} (w_2 - s_2) f_B\right\}}, \tag{A14}$$

where

$$f_B = 1 + C_\eta \frac{C_D C_\mu^* f_\mu}{\sqrt{2}} (\overline{w} - \overline{s}), \quad C_\eta = 100,$$

$$\overline{s} = \sqrt{2 s_{ij} s_{ij}}, \quad \overline{w} = \sqrt{2 w_{ij} w_{ij}}.$$

Acknowledgements

References

1. Gatski, T.B. and Speziale, C.G., On explicit algebraic stress models for complex turbulent flows. *J. Fluid Mech.* **254** (1993) 59–78.
2. Craft, T.J., Launder, B.E. and Suga, K., Development and application of a cubic eddy-viscosity model of turbulence. *Internat. J. Numer. Methods Fluids* **17** (1996) 108–115.
3. Apsley, D.D. and Leschziner, M.A., A new low-Reynolds-number nonlinear two- equation turbulence model for complex flows. *Internat. J. Heat Fluid Flow* **19** (1998) 209–222.
4. Rung, T., Fu, S. and Thiele, F., On the realizability of non-linear stress-strain relation for Reynolds-stress closures. *Flow, Turbulence and Combustion* **60** (1999) 333–359.
5. Wallin, S. and Johansson, A.V., An explicit algebraic Reynolds stress model for incompressible and compressible turbulent flows. *J. Fluid Mech.* **403** (2000) 89–132.
6. Abe, K., Jang, Y.-J. and Leschziner, M.A., An investigation of wall-anisotropy expressions and length-scale equations for non-linear eddy-viscosity models. *Internat. J. Heat Fluid Flow* **19** (2003) 181–198.
7. Haase, Brandsma, F., Elsholz, E., Leschziner, M.A. and Schwamborn, D. (eds.), *EUROVAL – A European Initiative on Validation of CFD Codes – Results of the EC/BRITE-EURAM Project EUROVAL, 1990–1992.* Notes on Numerical Fluid Mechanics, Vol. 42. Vieweg Verlag, Braunschweig (1993).
8. Haase, W., Chaput, E., Elsholz, E., Leschziner M.A. and Müller, U.R. (eds.), *ECARP: European Computational Aerodynamics Research Project. II: Validation of CFD Codes and Assessment of Turbulent Models.* Notes on Numerical Fluid Mechanics, Vol. 58. Vieweg Verlag, Braunschweig (1996).
9. Jakirlic, S., Jester-Zuerker, R. and Tropea, C. (eds.), *Proceedings 9th ERCOFTAC/IAHR/COST Workshop on Refined Turbulence Modelling*, Darmstadt (2001).
10. Sieverding, C.H., Turbulence modelling for unsteady flows in axial turbomachines. Final Report on Project TURMUNSFLAT (BE95-1698) (2000) submitted to the European Commission.
11. Apsley, D.D. and Leschziner, M.A., Advanced turbulence modelling of separated flow in a diffuser. *Flow, Turbulence and Combustion* **63** (2000), 81–112.
12. Temmerman, L. and Leschziner, M.A., Large eddy simulation of separated flow in a streamwise periodic channel constriction. In: Lindborg, E., Johansson, A., Eaton, J., Humphrey, J., Kasagai, N., Leschziner, M. and Sommerfeld, M. (eds.), *Proceedings 2nd Symposium on Turbulence and Shear-Flow Phenomena*, Stockholm (2001) pp. 399–404.
13. Mellen, C.P., Froehlich, J. and Rodi, W., Large eddy simulation of the flow over a periodic hill. In: Deville, M. and Owens, R. (eds.), *CD-Rom Proceedings 16th IMACS World Congress.* Lausanne, Switzerland (2000).
14. Temmerman, L., Leschziner, M.A., Mellen, C.P. and Froehlich, J., Investigation of wall-function approximations and subgrid-scale models in Large Eddy Simulation of separated flow in a channel with streamwise periodic constrictions. *Internat. J. Heat Fluid Flow* **24** (2003) 157–180.

15. Nicoud, F. and Ducros, F., Subgrid-scale modeling based on the square of the velocity gradient tensor. *Flow, Turbulence and Combustion* **62** (1999) 183–200.
16. Wilcox, D.C., Simulation of transition with a two-equation turbulence model. *AIAA J.* **32** (1994) 247–255.
17. Pope, S.B., A more general effective-viscosity hypothesis. *J. Fluid Mech.* **72** (1975), 331–340.
18. Launder, B.E. and Sharma, B.I., Application of the energy-dissipation model of turbulence to the calculation of flow near a spinning disc. *Lett. Heat Mass Transfer* **1** (1974) 131–138.
19. Speziale, C.G. and Xu, X.H., Towards the development of second-order closure models for nonequilibrium turbulent flows. *Internat. J. Heat Fluid Flow* **17** (1996) 238–244.
20. Loyau, H., Batten P. and Leschziner, M.A., Modeling shock/boundary-layer interaction with nonlinear eddy-viscosity closures. *Flow, Turbulence and Combustion* **60** (1998) 257–282.
21. Yap, C.R., Turbulent heat and momentum transfer in recirculating and impinging flows. Ph.D. Thesis, UMIST (1987).
22. Rodi, W., A new algebraic relation for calculating the Reynolds stresses. *Z. angew. Math. Mech.* **56** (1978) 219–221.
23. Speziale, C.G., Sarkar, S. and Gatski, T.B., Modeling the pressure-strain correlation of turbulence: An invariant dynamical systems approach. *J. Fluid Mech.* **227** (1991) 245–272.
24. Chen, H.C., Jang, Y.-J. and Han, J.C., Computation of heat transfer in rotating two-pass square channels by a second-moment closure model. *Internat. J. Heat Mass Transfer* **43** (2000) 1603–1616.
25. Lien, F.-S. and Leschziner, M.A., A general non-orthogonal collocated finite volume algorithm for turbulent flow at all speeds incorporating second-moment turbulence-transport closure, Part I: Computational implementation. *Comput. Methods Appl. Mech. Engrg.* **114** (1994) 123–148.
26. Lien, F.-L., Chen, W.L. and Leschziner, M.A., A multi-block implementation of non-orthogonal collocated finite-volume algorithm for complex turbulent flows. *Internat. J. Numer. Methods Fluids* **23** (1996) 567–588.
27. Lien, F.-S. and Leschziner, M.A., Upstream monotonic interpolation for scalar transport with application to complex turbulent flows. *Internat. J. Numer. Methods Fluids* **19** (1994) 527–548.
28. Leonard, B.P., A stable and accurate convective modeling procedure based on quadratic upstream interpolation. *Comput. Methods Appl. Mech. Engrg.* **19** (1979) 59–98.
29. Wilcox, D.C., Reassessment of the scale-determining equations for advanced turbulence models. *AIAA J.* **26** (1988) 1299–1310.